Nonequilibrium clumped isotope signals in microbial methane

Title: [max 135 char w/ spaces]

Nonequilibrium clumped isotope signals in microbial methane

A manuscript revised for submission to *Science* on 9 February 2015

Authors and affiliations:

David T. Wang[1,2], Danielle S. Gruen[1,2], Barbara Sherwood Lollar[3], Kai-Uwe Hinrichs[4], Lucy C. Stewart[5], James F. Holden[5], Alexander N. Hristov[6], John W. Pohlman[7,] Penny L. Morrill[8], Martin Könneke[4], Kyle B. Delwiche[9], Eoghan P. Reeves[1], Chelsea N. Sutcliffe[3], Daniel J. Ritter[10], Jeffrey S. Seewald[2], Jennifer C. McIntosh[10], Harold F. Hemond[9], Michael D. Kubo[11], Dawn Cardace[12], Tori M. Hoehler[11], and Shuhei Ono[1,*]

[1]Department of Earth, Atmospheric and Planetary Sciences, Massachusetts Institute of Technology, Cambridge, Massachusetts 02139, USA.
[2]Marine Chemistry and Geochemistry Department, Woods Hole Oceanographic Institution, Woods Hole, Massachusetts 02543, USA.
[3]Department of Earth Sciences, University of Toronto, Toronto, Ontario M5S 3B1, Canada.
[4]MARUM Center for Marine Environmental Sciences and Department of Geosciences, University of Bremen, Bremen D-28359, Germany.
[5]Department of Microbiology, University of Massachusetts, Amherst, Massachusetts 01003, USA.
[6]Department of Animal Science, Pennsylvania State University, University Park, Pennsylvania 16802, USA.
[7]U.S. Geological Survey, Woods Hole Coastal and Marine Science Center, Woods Hole, Massachusetts 02543, USA.
[8]Department of Earth Sciences, Memorial University of Newfoundland, St John's, Newfoundland and Labrador A1B 3X5, Canada.
[9]Department of Civil and Environmental Engineering, Massachusetts Institute of Technology, Cambridge, Massachusetts 02139, USA.
[10]Department of Hydrology and Water Resources, University of Arizona, Tucson, Arizona 85721, USA.
[11]NASA Ames Research Center, Moffett Field, California 94035, USA.
[12]Department of Geosciences, University of Rhode Island, Kingston, Rhode Island 02881, USA.

* To whom correspondence should be addressed:

S. Ono
Department of Earth, Atmospheric, and Planetary Sciences
Massachusetts Institute of Technology
77 Massachusetts Ave, Cambridge, MA 02139
(617) 253-0474
sono@mit.edu

Abstract [max 125 words]

Methane is a key component in the global carbon cycle with a wide range of anthropogenic and natural sources. Although isotopic compositions of methane have traditionally aided source identification, the abundance of its multiply-substituted "clumped" isotopologues, e.g., $^{13}CH_3D$, has recently emerged as a proxy for determining methane-formation temperatures; however, the impact of biological processes on methane's clumped isotopologue signature is poorly constrained. We show that methanogenesis proceeding at relatively high rates in cattle, surface environments, and laboratory cultures exerts kinetic control on $^{13}CH_3D$ abundances and results in anomalously elevated formation temperature estimates. We demonstrate quantitatively that H_2 availability accounts for this effect. Clumped methane thermometry can therefore provide constraints on the generation of methane in diverse settings, including continental serpentinization sites and ancient, deep groundwaters.

122 words

Carbon ($^{13}C/^{12}C$) and hydrogen (D/H) isotope ratios of methane are widely applied for distinguishing microbial from thermogenic methane in the environment (*1–7*) as well as for apportioning pathways of microbial methane production (*8–10*). This bulk isotope approach, however, is largely based on empirical observations, and different origins of methane often yield overlapping characteristic isotope signals (*3*, *7*, *11–13*). Beyond conventional bulk isotope ratios, it has become possible to precisely measure the abundance of multiply-substituted "clumped" isotopologues (e.g., $^{13}CH_3D$) (*14*, *15*). In particular, abundance of clumped isotopes promises to yield information about the temperature at which C-H bonds were formed or last equilibrated [(*14*); fig. S1]. Indeed, formation temperatures of both thermogenic and microbial methane in natural gas reservoirs can be estimated on the basis of clumped isotopologues (*16*). The mechanisms by which isotopologues attain distributions consistent with thermodynamic equilibrium, however, remain unclear because bulk methane isotopes ($\delta^{13}C$ and δD) often reflect kinetic isotope fractionations (*13*, *17*), and H-isotope exchange between methane and water is sluggish (*18*).

To test if clumped methane thermometry can be widely applied for methane sources beyond natural gas reservoirs, we examined methane samples from diverse systems, including lakes, wetlands, cow rumen, laboratory cultures of methanogenic microbes, and geological settings that may support abiogenic methane production as well as thermogenic and microbial sources, including continental serpentinization sites and deep fracture fluids. We measured the relative abundances of four methane isotopologues ($^{12}CH_4$, $^{13}CH_4$, $^{12}CH_3D$ and $^{13}CH_3D$) using a recently-developed tunable laser spectroscopy technique (*14*, *19*).

Our measurements for dominantly-thermogenic gases from the Marcellus and Utica Shales (*1*, *20*) yielded $\Delta^{13}CH_3D$-based temperatures of 147^{+25}_{-22} °C and 160^{+29}_{-25} °C, respectively. The clumped-isotope temperature for the Marcellus Shale sample is comparable to, although slightly lower than, estimates by Stolper et al. (*16*) of 179–207 °C (Fig. 1). In addition, microbial methane in pore waters and gas hydrates from northern Cascadia margin sediments (*3*), and from wells producing from coal seams in the Powder River Basin (*2*, *21*) yielded $\Delta^{13}CH_3D$ temperatures of 12-42 °C and 35–52 °C, respectively. These are consistent with their expected low formation temperatures. Furthermore, thermogenic methane sampled from a hydrothermal vent in the Guaymas Basin, Gulf of California (*6*), yielded $\Delta^{13}CH_3D$ temperature of 326^{+170}_{-95} °C, within error of the measured vent temperature [299 °C (*22*)]. Therefore, our data provide independent support of the hypothesis that $^{13}CH_3D$ abundance reflects the temperature at which methane is generated in these sedimentary basins (*16*).

In contrast, we found that methane sampled from lakes, a swamp, and the rumen of a cow carry $^{13}CH_3D$ signals that correspond to anomalously high $\Delta^{13}CH_3D$ temperatures (139–775 °C, Fig. 1A), i.e., well above the environmental temperatures (<40 °C). Such signals are clearly not controlled by equilibrium. Notably, a positive correlation between $\Delta^{13}CH_3D$ and the extent of D/H fractionation between methane and environmental water [$\varepsilon_{methane/water}$ (*23*); Fig. 2] suggests a strong link between isotopologue (i.e., $^{13}CH_3D$) and isotope (D/H) disequilibria. In contrast, the above mentioned methane samples from sedimentary basins appear to have attained hydrogen-isotope equilibrium with associated waters at or near the temperatures indicated by the $\Delta^{13}CH_3D$ data (Fig. 2).

To confirm these observations from the natural environment, we demonstrated that strong disequilibrium $^{13}CH_3D$ signals are also produced by cultures of methanogenic archaea in the laboratory (Fig. 3). Thermophilic methanogens cultured at 40 to 85 °C produced methane with $\Delta^{13}CH_3D$ values from +0.5 to

+2.3‰ (corresponding to $\Delta^{13}CH_3D$ temperatures of 216–620 °C), and mesophilic methanogens cultured at ambient temperature produced methane with conspicuously "anti-clumped" signatures (i.e., values of $\Delta^{13}CH_3D < 0‰$, for which no apparent temperature can be expressed) as low as −1.3‰ (Fig. 3). Methane from cultures is also characterized by large kinetic D/H fractionation with respect to water (*17*, *24*). Because laboratory cultures are grown under optimal conditions (high-H_2 and high-CO_2), these anti-clumped $\Delta^{13}CH_3D$ and low $\varepsilon_{methane/water}$ values are primarily expressions of kinetic isotope effects. Consequently, the distribution of samples with $\Delta^{13}CH_3D$ and $\varepsilon_{methane/water}$ values in Fig. 2 can be explained by microbial methanogenesis operating on a spectrum between fully kinetic (low $\Delta^{13}CH_3D$ and low $\varepsilon_{methane/water}$) and equilibrium (high $\Delta^{13}CH_3D$ and high $\varepsilon_{methane/water}$) end-members.

We constructed a mathematical framework to describe the controls on the correlation of $\Delta^{13}CH_3D$ and $\varepsilon_{methane/water}$ signals from hydrogenotrophic methanogenesis. The model largely follows those developed for microbial sulfate reduction (*25*, *26*) and predicts the isotopologue compositions of product methane as a result of a series of enzymatic reactions [fig. S4; (*19*)]. Using isotope fractionation factors estimated from theory, experiments and observations as input parameters [table S3; (*19*)], our model reproduces the observed correlation between $\Delta^{13}CH_3D$ and $\varepsilon_{methane/water}$ of natural samples (Fig. 2). The isotopologue compositions of product methane reflect the degree of metabolic reversibility. Fully reversible reactions yield equilibrium end-members (*27*), while irreversible reactions result in kinetic (disequilibrium) end-member signals. In this model, the reversibility is linked to available free energy (*26*, *27*), in this case expressed as H_2 concentration ($[H_2]$). The model can explain the relationship among $[H_2]$, $\varepsilon_{methane/water}$ (*28*) and $\Delta^{13}CH_3D$ via Michaelis-Menten kinetics, and predicts the observed patterns in diverse settings ranging from marine sediments (low $[H_2]$, high $\Delta^{13}CH_3D$ and $\varepsilon_{methane/water}$) to bovine rumen (high $[H_2]$, low $\Delta^{13}CH_3D$ and $\varepsilon_{methane/water}$) (Fig. 4). We note that mixing of methane sources with different $\delta^{13}C$ and δD values or oxidation of methane could also alter the relationships over the primary signal of microbial methanogenesis (*19*). Likewise, inheritance of clumping signals from precursor organic substrates (e.g., via acetoclastic or methylotrophic methanogenesis), cannot be entirely ruled out and await experimental validation.

We showed above that the combination of $\Delta^{13}CH_3D$ and $\varepsilon_{methane/water}$ values provides mechanistic constraints on whether methane was formed under kinetic vs. near-equilibrium conditions. Next, we used this framework to place constraints on the origins of methane at two sites of present-day serpentinization in Phanerozoic ophiolites [The Cedars (*29*) and Coast Range Ophiolite Microbial Observatory, CROMO (*30*)] in northern California, and in deep (> 2 km below surface) fracture fluids with billion year-residence times in the Kidd Creek mine, Canada (*5*, *31*).

Methane-rich gases in groundwater springs associated with serpentinization at The Cedars yielded anti-clumped $\Delta^{13}CH_3D$ signals (−3‰) with low $\varepsilon_{methane/water}$ values (Figs. 1A and 2). The data plot along the microbial (kinetic) trend defined in Fig. 2, supporting a previous hypothesis that methane at The Cedars is being produced by active microbial methanogenesis (*29*). The exceptionally high H_2 concentration (up to 50% by volume in bubbles) and low E_h (ca. −600 mV) at The Cedars indicate the massive excess of electron donor. This, along with severe inorganic carbon limitation [due to high pH (>11) and precipitation of carbonate minerals (*29*)], drives the formation of methane carrying strong kinetic imprints, consistent with the observed anti-clumped $\Delta^{13}CH_3D$ signals (Fig. 4).

Despite the similarity in geologic setting, methane associated with serpentinization at CROMO (*30*) revealed very different $\Delta^{13}CH_3D$ values, which correspond to low apparent temperatures (42–76 °C) and plot close to the equilibrium line (Fig. 2). While the conventional $\delta^{13}C$ and δD values of methane from CROMO are nearly identical to those of the Utica Shale sample (Fig. 1B), methane at CROMO carries much higher $\Delta^{13}CH_3D$ values (Fig. 1A). The origin of methane at the CROMO site remains unresolved (*30*), but the comparably high $\Delta^{13}CH_3D$ values at CROMO suggest methane here could be sourced from a mixture of thermogenic and microbial methane. Alternatively, lower H_2 availability at CROMO, compared to The Cedars (table S4), may support microbial methanogenesis under near-equilibrium conditions (Fig. 4). Regardless, the different isotopologue signatures in methane from CROMO vs. The Cedars demonstrate that distinct processes contribute to methane formation in these two serpentinization systems.

Deep, ancient fracture fluids in the Kidd Creek mine in the Canadian Shield (*31*) contain copious quantities of both dissolved methane and hydrogen (*5*). The Kidd Creek methane occupies a distinct region in the $\Delta^{13}CH_3D$ vs. $\varepsilon_{methane/water}$ diagram (Fig. 2), due to strong D/H disequilibria between methane and water (*4*) and low $\Delta^{13}CH_3D$ temperature signals of 56–90 °C that are consistent with other temperature estimates for these groundwaters (*4*). Although the specific mechanisms by which the proposed abiotic hydrocarbons at Kidd Creek are generated remain under investigation (*5*, *32*), the distinct isotopologue signals provide further support for the hypothesis that methane here is neither microbial nor thermogenic.

Our results demonstrate that measurements of $^{13}CH_3D$ provide information beyond the simple formation temperature of methane. Combination of methane/water hydrogen-isotope fractionation and $^{13}CH_3D$ abundance enables the differentiation of methane that has been formed at extremely low rates in the subsurface (*3*, *21*, *27*) from methane formed in cattle and surface environments in which methanogenesis proceeds at comparatively high rates (*33*, *34*).

word count: 1441 main text [target 1500]

Fig. 1. Isotopologue compositions of methane samples. **(A)** $\Delta^{13}CH_3D$ plotted against δD. The $\Delta^{13}CH_3D$ temperature scale corresponds to calibration in fig. S1. Error bars are 95% confidence intervals (table S1). Data from (*16*) were scaled to their corresponding $\Delta^{13}CH_3D$ values (*15*). The shaded area represents the temperature range within which microbial life has been demonstrated to date (*35*). The hatched line represents $\Delta^{13}CH_3D$ = 0‰ (T → ∞); data plotting below this line cannot yield corresponding apparent temperatures. **(B)** $\delta^{13}C$ plotted against δD, showing characteristic fields for different methane sources from (*13*).

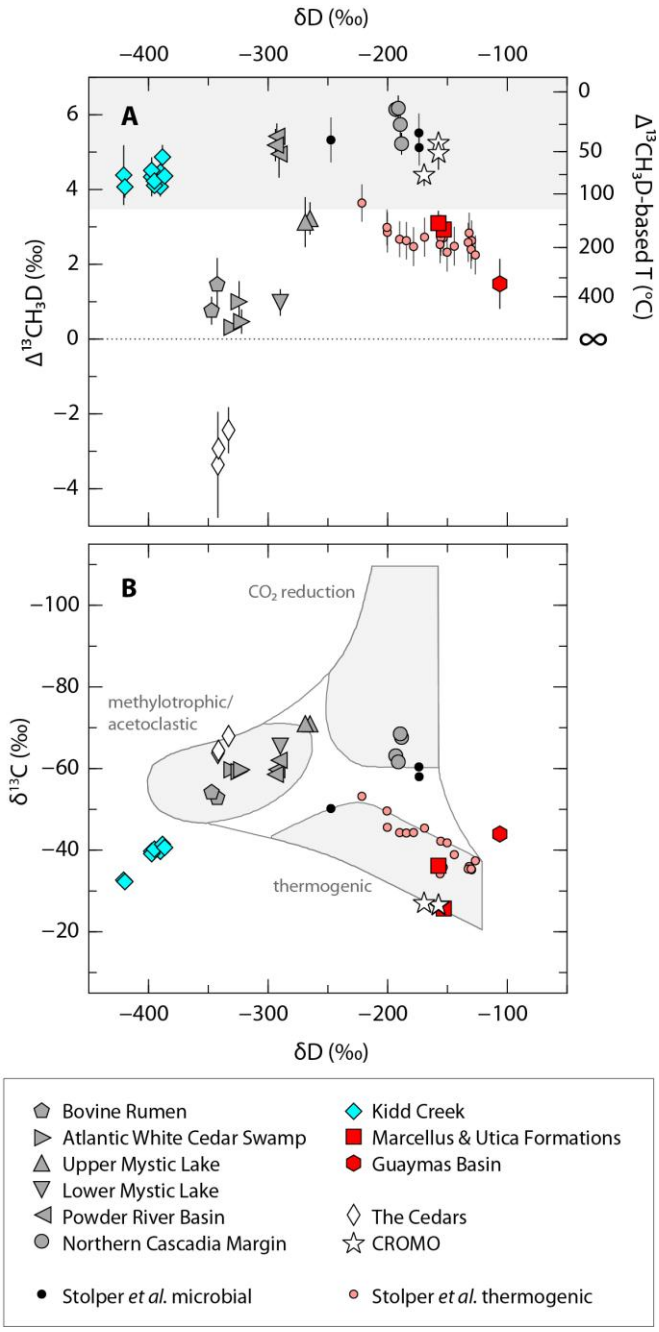

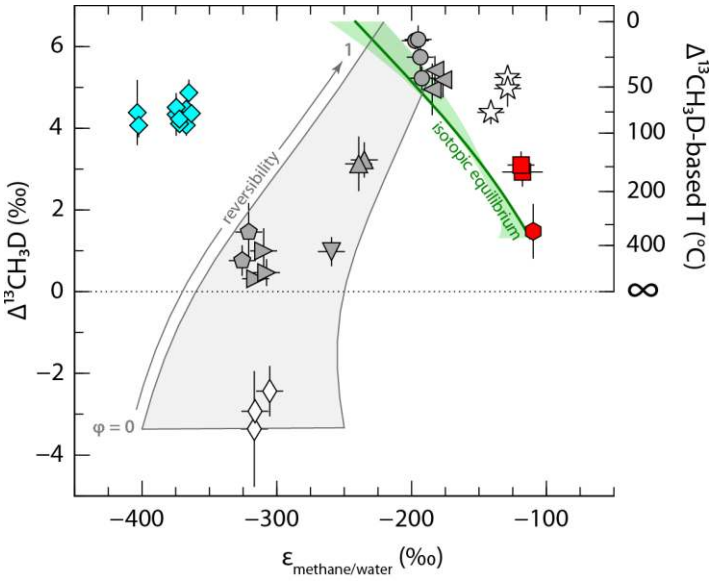

Fig. 2. Extent of clumped- and hydrogen-isotopic disequilibria in methane. Symbols and vertical error bars are the same as those in Fig. 1. Horizontal error bars represent uncertainties on estimates of $\varepsilon_{methane/water}$ [(*23*); table S4]. The solid green curve represents isotopic equilibrium, with the $\varepsilon_{methane/water}$ calibration given by ref. 36. Green shading represents ranges of $\varepsilon_{methane/water}$ calibrations from published reports (fig. S3). Gray shading represents model predictions from this study, for microbial methane formed between 0 and 40 °C. Metabolic reversibility (φ) increases from bottom (φ = 0, fully-kinetic) to top (φ → 1, equilibrium) within this field (*19*).

Fig. 3. $\Delta^{13}CH_3D$ values of methane produced by hydrogenotrophic methanogens in batch cultures reflect kinetic effects. Data and error bars are from table S2. The green line represents clumped isotopologue equilibrium (i.e., samples for which $\Delta^{13}CH_3D$ temperature is equal to growth temperature; fig. S1).

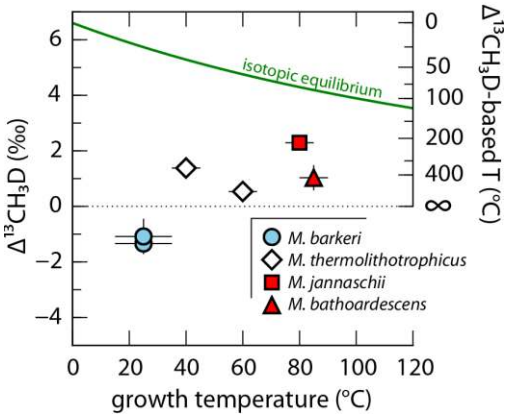

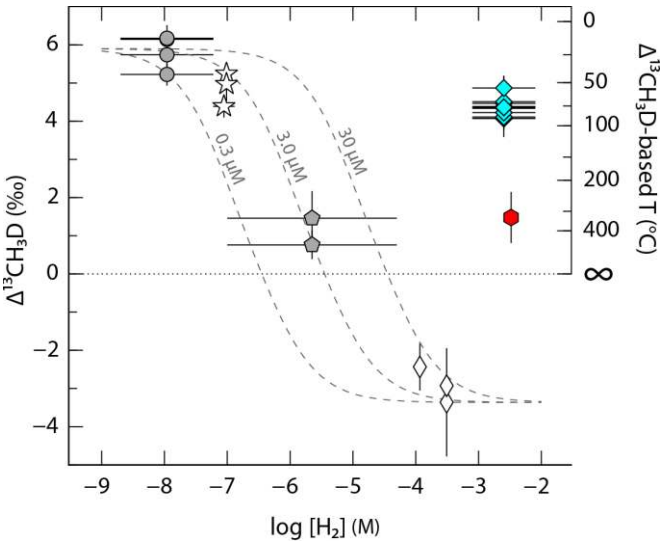

Fig. 4. Relationships between $\Delta^{13}CH_3D$ and H_2 concentration for microbial methane. Symbols and vertical error bars are the same as in Fig. 1. The H_2 data are from table S4; when a range of $[H_2]$ values is given, points are plotted at the geometric mean of the maximum and minimum values. Dashed lines represent model predictions for microbial methane produced at 20 °C, calculated using K_M's of 0.3, 3.0, and 30 μM H_2. Data for samples of non-dominantly-microbial methane from Guaymas Basin and Kidd Creek are plotted for comparison.

References and Notes

1. F. J. Baldassare, M. A. McCaffrey, J. A. Harper, A geochemical context for stray gas investigations in the northern Appalachian Basin: Implications of analyses of natural gases from Neogene-through Devonian-age strata, *Am. Assoc. Pet. Geol. Bull.* **98**, 341–372 (2014).
2. R. M. Flores, C. A. Rice, G. D. Stricker, A. Warden, M. S. Ellis, Methanogenic pathways of coal-bed gas in the Powder River Basin, United States: the geologic factor, *Int. J. Coal Geol.* **76**, 52–75 (2008).
3. J. Pohlman, M. Kaneko, V. Heuer, R. Coffin, M. Whiticar, Methane sources and production in the northern Cascadia margin gas hydrate system, *Earth Planet. Sci. Lett.* **287**, 504–512 (2009).
4. B. Sherwood Lollar *et al.*, Isotopic signatures of CH_4 and higher hydrocarbon gases from Precambrian Shield sites: A model for abiogenic polymerization of hydrocarbons, *Geochim. Cosmochim. Acta* **72**, 4778–4795 (2008).
5. B. Sherwood Lollar, T. Westgate, J. Ward, G. Slater, G. Lacrampe-Couloume, Abiogenic formation of alkanes in the Earth's crust as a minor source for global hydrocarbon reservoirs, *Nature* **416**, 522–524 (2002).
6. J. Welhan, J. Lupton, Light hydrocarbon gases in Guaymas Basin hydrothermal fluids: thermogenic versus abiogenic origin, *Am. Assoc. Pet. Geol. Bull.* **71**, 215–223 (1987).
7. M. J. Whiticar, A geochemial perspective of natural gas and atmospheric methane, *Org. Geochem.* **16**, 531–547 (1990).
8. R. A. Burke Jr., C. S. Martens, W. M. Sackett, Seasonal variations of D/H and $^{13}C/^{12}C$ ratios of microbial methane in surface sediments, *Nature* **332**, 829–831 (1988).
9. C. K. McCalley *et al.*, Methane dynamics regulated by microbial community response to permafrost thaw, *Nature* **514**, 478–481 (2014).
10. M. J. Whiticar, E. Faber, M. Schoell, Biogenic methane formation in marine and freshwater environments: CO_2 reduction vs. acetate fermentation—Isotope evidence, *Geochim. Cosmochim. Acta* **50**, 693–709 (1986).
11. G. Etiope, B. Sherwood Lollar, Abiotic methane on Earth, *Rev. Geophys.* **51**, 276–299 (2013).
12. M. Schoell, Multiple origins of methane in the earth, *Chem. Geol.* **71**, 1–10 (1988).
13. M. J. Whiticar, Carbon and hydrogen isotope systematics of bacterial formation and oxidation of methane, *Chem. Geol.* **161**, 291–314 (1999).
14. S. Ono *et al.*, Measurement of a doubly-substituted methane isotopologue, $^{13}CH_3D$, by tunable infrared laser direct absorption spectroscopy, *Anal. Chem.* **86**, 6487–6494 (2014).
15. D. A. Stolper *et al.*, Combined ^{13}C-D and D-D clumping in methane: methods and preliminary results, *Geochim. Cosmochim. Acta* **126**, 169–191 (2014).
16. D. A. Stolper *et al.*, Formation temperatures of thermogenic and biogenic methane, *Science* **344**, 1500–1503 (2014).
17. D. L. Valentine, A. Chidthaisong, A. Rice, W. S. Reeburgh, S. C. Tyler, Carbon and hydrogen isotope fractionation by moderately thermophilic methanogens, *Geochim. Cosmochim. Acta* **68**, 1571–1590 (2004).
18. E. P. Reeves, J. S. Seewald, S. P. Sylva, Hydrogen isotope exchange between *n*-alkanes and water under hydrothermal conditions, *Geochim. Cosmochim. Acta* **77**, 582–599 (2012).
19. Materials and methods are available as supplementary materials on *Science* Online.
20. R. Burruss, C. Laughrey, Carbon and hydrogen isotopic reversals in deep basin gas: Evidence for limits to the stability of hydrocarbons, *Org. Geochem.* **41**, 1285–1296 (2010).
21. B. L. Bates, J. C. McIntosh, K. A. Lohse, P. D. Brooks, Influence of groundwater flowpaths, residence times and nutrients on the extent of microbial methanogenesis in coal beds: Powder River Basin, USA, *Chem. Geol.* **284**, 45–61 (2011).
22. E. P. Reeves, J. M. McDermott, J. S. Seewald, The origin of methanethiol in midocean ridge hydrothermal fluids, *Proc. Natl. Acad. Sci. U. S. A.* **111**, 5474–5479 (2014).
23. The abundance of $^{13}CH_3D$ is captured by a metric, $\Delta^{13}CH_3D$, which quantifies its deviation from a random distribution of isotopic substitutions amongst all isotopologues in a sample of methane: $\Delta^{13}CH_3D = \ln Q$, where Q is the reaction quotient of the isotope exchange reaction: $^{13}CH_4 + {}^{12}CH_3D \rightleftharpoons {}^{13}CH_3D + {}^{12}CH_4$, where the δ-values are conventional isotopic notation, e.g., $\delta D = (D/H)_{sample}/(D/H)_{reference} - 1$. Mass spectrometric measurements yield Δ_{18}, a parameter that quantifies the combined abundance of $^{13}CH_3D$ and $^{12}CH_2D_2$. For most natural samples of methane, Δ_{18} is expected to be directly-relatable to $\Delta^{13}CH_3D$ as measured by laser spectroscopy. The D/H fractionation between methane and environmental water is defined as $\varepsilon_{methane/water} = (D/H)_{methane}/(D/H)_{water} - 1$.
24. M. Balabane, E. Galimov, M. Hermann, R. Letolle, Hydrogen and carbon isotope fractionation during experimental production of bacterial methane, *Org. Geochem.* **11**, 115–119 (1987).
25. C. Rees, A steady-state model for sulphur isotope fractionation in bacterial reduction processes, *Geochim. Cosmochim. Acta* **37**, 1141–1162 (1973).
26. B. A. Wing, I. Halevy, Intracellular metabolite levels shape sulfur isotope fractionation during microbial sulfate respiration, *Proc. Natl. Acad. Sci. U. S. A.* (2014).
27. T. Holler *et al.*, Carbon and sulfur back flux during anaerobic microbial oxidation of methane and coupled sulfate reduction, *Proc. Natl. Acad. Sci. U. S. A.* **108**, E1484–E1490 (2011).
28. R. A. Burke Jr., Possible influence of hydrogen concentration on microbial methane stable hydrogen isotopic composition, *Chemosphere* **26**, 55–67 (1993).
29. P. L. Morrill *et al.*, Geochemistry and geobiology of a present-day serpentinization site in California: The Cedars, *Geochim. Cosmochim. Acta* **109**, 222–240 (2013).

30. D. Cardace *et al.*, Establishment of the Coast Range ophiolite microbial observatory (CROMO): drilling objectives and preliminary outcomes, *Sci. Dril.* **16**, 45–55 (2013).
31. G. Holland *et al.*, Deep fracture fluids isolated in the crust since the Precambrian era, *Nature* **497**, 357–360 (2013).
32. B. Sherwood Lollar, T. C. Onstott, C. J. Ballentine, G. Lacrampe-Couloume, The contribution of the Precambrian continental lithosphere to global hydrogen production, *Nature* **516**, 379–382 (2014).
33. K. A. Johnson, D. E. Johnson, Methane emissions from cattle., *J. Anim. Sci.* **73**, 2483–2492 (1995).
34. C. Varadharajan, H. F. Hemond, Time-series analysis of high-resolution ebullition fluxes from a stratified, freshwater lake, *J. Geophys. Res.* **117**, G02004 (2012).
35. K. Takai *et al.*, Cell proliferation at 122 °C and isotopically heavy CH_4 production by a hyperthermophilic methanogen under high-pressure cultivation, *Proc. Natl. Acad. Sci. U. S. A.* **105**, 10949–10954 (2008).
36. Y. Horibe, H. Craig, D/H fractionation in the system methane-hydrogen-water, *Geochim. Cosmochim. Acta* **59**, 5209–5217 (1995).

Acknowledgments. We thank J. Hayes, R. Summons, A. Whitehill, S. Zaarur, C. Ruppel, L.T. Bryndzia, N. Blair, D. Vinson, K. Nealson, and M. Schrenk for discussions; W. Olszewski, D. Nelson, G. Lacrampe-Couloume, and B. Topçuoğlu for technical assistance; A. Whitehill, G. Luo, A. Apprill, K. Twing, W. Brazelton, A. Wray, J. Oh, A. Rowe, G. Chadwick, and A. Rietze for assistance in the field; R. Michener for the δD_{water} analyses; and R. Dias (USGS) for sharing the NGS samples. We thank R. Raiche and D. McCrory, S. Moore (Homestake Mining Co.) and the staff of the McLaughlin Natural Reserve, and Shell and other operators for access to samples. Grants from the National Science Foundation (EAR-1250394 to S.O. and EAR-1322805 to J.C.M.), N. Braunsdorf and D. Smit of Shell PTI/EG (to S.O.), the Deep Carbon Observatory (to S.O., B.S.L., M.K., and K.-U.H.), the Natural Sciences and Engineering Research Council of Canada (to B.S.L.), and the Gottfried Wilhelm Leibniz Program of the Deutsche Forschungsgemeinschaft (HI 616-14-1 to K.-U.H. and M.K.) supported this study. D.T.W. was supported by a National Defense Science and Engineering Graduate Fellowship. D.S.G. was supported by the Neil and Anna Rasmussen Foundation Fund, the Grayce B. Kerr Fellowship, and a Shell-MITEI Graduate Fellowship. Any use of trade, firm, or product names is for descriptive purposes only and does not imply endorsement by the U.S. Government. All data used to support the conclusions in this manuscript are provided in the supplementary materials.

Author Contributions. D.T.W. and S.O. developed the methods, analyzed data, and performed modeling. D.T.W. and D.S.G. performed isotopic analyses. D.S.G., L.C.S., J.F.H., M.K., K.-U.H., and S.O. designed and/or conducted microbiological experiments. D.T.W., D.S.G., B.S.L., P.L.M., K.B.D., A.N.H., C.N.S., M.D.K., D.J.R., J.C.M., D.C., and S.O. designed and/or executed the field sampling campaigns. D.T.W. and S.O. wrote the manuscript with input from all authors.

Supplementary Materials

Supplementary Materials for

Unique non-equilibrium clumped isotope signals in microbial methane

David T. Wang, Danielle S. Gruen, Barbara Sherwood Lollar, Kai-Uwe Hinrichs, Lucy C. Stewart, James F. Holden, Alexander N. Hristov, John W. Pohlman, Penny L. Morrill, Martin Könneke, Kyle B. Delwiche, Eoghan P. Reeves, Chelsea N. Sutcliffe, Daniel J. Ritter, Jeffrey S. Seewald, Jennifer C. McIntosh, Harold F. Hemond, Michael D. Kubo, Dawn Cardace, Tori M. Hoehler, and Shuhei Ono*

*correspondence to: sono@mit.edu

This PDF file includes:

Materials and Methods

Animal care

Sampling of methane from bovine subjects was conducted according to guidelines established by the Institutional Animal Care and Use Committee at the Pennsylvania State University.

Cultivation of methanogens

We established batch culture incubations of *Methanocaldococcus bathoardescens*, *Methanocaldococcus jannaschii*, *Methanothermococcus thermolithotrophicus,* and *Methanosarcina barkeri* under atmospheres containing 80% H_2 and 20% CO_2. Cultures of *M.jannaschii* (*37*) and *M. barkeri* (strain DSM-800) (*38*) were purchased from the German Collection of Microorganisms and Cell Cultures (DSMZ, Braunschweig, Germany). *Methanocaldococcus bathoardescens* (formerly known as strain JH146) is a recently-isolated hyperthermophilic, obligate hydrogenotrophic methanogen with exhibiting optimum growth at 82 °C (*39*, *40*). The growth medium for *M.jannaschii, M. thermolithotrophicus,* and *M. bathoardescens* was prepared according to the recipe for DSMZ medium 282, amended with 1g/L NaS_2O_3. Aliquots of the medium (50 ml) were transferred into 160 ml glass serum vials stoppered with blue butyl rubber septa, and the headspace was filled with 2 atm H_2:CO_2 (80:20). The growth medium for *M. barkeri* was prepared according to the recipe for DSMZ medium 120, and the headspace was filled with 1.5 atm H_2:CO_2 (80:20). Cultures were incubated at ambient temperature (*M. barkeri*, in duplicate), at 40 and 60 °C (*M. thermolithotrophicus*), at 80 °C (*M.jannaschii*), or at 85 °C (*M. bathoardescens*).

Sample purification procedures

To extract methane quantitatively from gas samples, we applied a preparative-gas chromatography technique modified from Alei et al. (*41*). In brief, a sample is introduced into a stream of helium. Water is removed by passing the sample through a U-trap cooled to −80 °C, and then CH_4, air (N_2, O_2, Ar), CO, CO_2, and C_{2+} are cryofocused onto a U-trap packed with activated charcoal and held at −196 °C. The condensed gases are then released by rapid heating to 120 °C, passed through a packed column (Carboxen-1000, 5' × 1/8", Supelco) held at 30 °C under helium flow (~25 ml/min), and monitored using thermal conductivity detection. The methane peak is trapped on a U-trap packed with silica gel and held at −196 °C; this is analogous to a "heart-cut" technique used previously for preparative separation of SF_6 for isotopic analysis (*42*). After elution of methane, the column is baked at 180 °C under a reversed (backflushed) flow of helium to remove CO_2 and C_{2+}.

This sample preparation procedure induces small fractionations in $\delta^{13}C$ and δD of methane of 0.09 ± 0.06‰ and 0.20 ± 0.02‰, respectively (1*s*, *n* = 4); these effects are minor compared to the magnitude of $\delta^{13}C$ and δD variations in nature. Critically, our procedure does not discernibly alter the $\Delta^{13}CH_3D$ value; the average difference between samples treated vs. not treated with this procedure was −0.09 ± 0.16‰ (1*s*, *n* = 4), which is not significantly different from zero.

Reporting of $\delta^{13}C$ and δD values

The $\delta^{13}C$ and δD values we report have been calibrated relative to PDB and SMOW, respectively, by measuring samples of NGS-1 and NGS-3. These reference values for $\delta^{13}C$ and δD are, respectively,

−29.0‰ and −138‰ for NGS-1, and −72.8‰ and −176‰ for NGS-3, as determined (*43*). The results for the calibration samples are shown in table S5.

Heated gas calibrations

To confirm and extend a previously-published temperature calibration (*14*), Pyrex tubes containing samples of methane with a range of $\delta^{13}C$ (−82 to −34‰ vs. PDB) and δD (−615 to +220‰ vs. SMOW) were prepared. These samples were heated over Pt catalyst at temperatures of 150, 170, 250, and 400 °C (n = 1, 3, 28, and 7, respectively). Gases were heated for 110 d, 73–76 d, 2–24 d, and 16–60 h, respectively, following a procedure described in Ono et al. (*14*).

When the theoretical methane equilibrium line is aligned to samples heated at 150, 170, and 250 °C, measurements of the samples heated at 400 °C yielded slightly lower $\Delta^{13}CH_3D$ temperatures (347^{+42}_{-36} °C), perhaps because quenching the reaction may take longer than the time for exchange over catalyst at ~400 °C. As a result, the data from the 400 °C heated gases were not used in aligning the calibration in fig. S1.

The theoretical equilibrium line we calculated agrees well with published results from both path-integral Monte Carlo simulations (*44*) and harmonic oscillator assumption-based approaches (*44–46*). The results of results of calculations employing an anharmonic correction, however, differ slightly from results of models assuming harmonic-oscillator behavior [by ~0.3‰ near room temperature (*44*, *45*)]. Fig. S1 shows results from recent studies (*44–46*) comparing multiple computational approaches for estimating the temperature-dependence of the equilibrium $\Delta^{13}CH_3D$ value. We note that while the uncertainty in the theoretical curve is similar in magnitude to our analytical uncertainty, particularly at temperatures <100 °C, these calibration uncertainties do not affect the conclusions drawn in this study.

Spectroscopic procedures

Samples of purified methane were analyzed using a tunable-infrared laser direct absorption spectrometer (Aerodyne Research, Billerica, Massachusetts) housed at MIT as described in Ono et al. (*14*), with improvements described here. All measurements reported in this paper were obtained at a nominal cell pressure of ca. 1.0 torr, instead of the 0.8 torr used in Ono et al. (*14*). We have found that this higher cell pressure gave improved measurement stability. As suggested previously (*14*), there is a small offset in the baseline underneath the $^{13}CH_3D$ absorption line, likely due to the insufficient accuracy of the Voigt profile for describing the contribution from tailing of adjacent $^{12}CH_4$ peak. We have used all 250 °C experiments shown in fig. S2 to generate a single set of correction factors, which show no observable drift during the time period all measurements were made.

Long-term internal reproducibility was evaluated by repeated analysis of methane from a commercially-sourced gas cylinder over a period of >4 months, yielding precisions for $\delta^{13}C$ of ±0.02‰, δD of ±0.02‰, and $\Delta^{13}CH_3D$ of ±0.08‰ (1s, n = 13). As described in Ono et al. (*14*), each measurement run consists of multiple acquisition cycles (a cycle is defined as one comparison of a sample/standard pair). The number of cycles (N_{cycles}) depends on sample size, but is typically greater than 5. In this paper, $\Delta^{13}CH_3D$ measurements are reported as mean ± 95% confidence intervals (CI) on the average of all isotope ratios obtained for each acquisition cycle over a measurement run, calculated as: $95\%\ \mathrm{CI} = tinv(\alpha, \mathrm{df}) \cdot \frac{s}{\sqrt{N_{\mathrm{cycles}}}}$, where *tinv* is the two-tailed inverse of the Student's *t*-distribution for α = 0.05 with $N_{cycles} - 1$

degrees of freedom (df), and [$s \geq 0.27$‰ (this value is the standard deviation on measurements for which 24 or more cycles were taken (0.27 ± 0.08‰, 1s on 1s, n = 7), and thus estimates the internal precision of the instrument]. The uncertainties on $\Delta^{13}CH_3D$ values reported for samples in tables S1, S2, and S5 also contain the propagated uncertainty in the $\Delta^{13}CH_3D$ value of our methane reference gas (AL1). Based on the calibration shown in fig. S1, we determined that AL1 carries a $\Delta^{13}CH_3D$ value of +2.41 ± 0.08‰ (95% CI).

To enable analysis of small (ca. 1 cm^3 STP) methane samples, we have developed a cold trap system to recover and recycle methane samples for re-analysis. In the current study, the only sample for which this recycling method was used was "Sally-1", a sample from a bovine rumen (table S1).

Model of isotopologue systematics during microbial methanogenesis

A mathematical model was constructed to describe isotopologue compositions of methane produced from microbial methanogenesis (fig. S4). To allow for the use of data from studies on experimental and natural systems as input parameters, our model simplifies the representation of the biochemistry involved in the microbial generation of methane, and only considers the production of methane via reduction of CO_2.

The model describes methanogenesis in six steps, and using an assumption of steady-state intermediate compositions, solves for the abundances of ^{13}C- and D-substituted isotopologues of product CH_4 and of four intermediate species (fig. S4). The first step (1) is the uptake of CO_2 into the cell, and the last step (6) is export of CH_4 out of the cell; we assume that neither of these steps discriminates against isotopes or between isotopologues. Inside the cell, the reduction of CO_2 to CH_4 is treated in four steps (steps #2–5), where each step corresponds to the addition of one hydrogen (*47*).

The main variable input in our model is metabolic reversibility, which is defined as the ratio of backwards to forwards fluxes ($\varphi_n = w_n/v_n$) through an enzymatically-mediated reaction sequence (*25*, *48*). The reversibility is constrained by two end-members, which represent fully-irreversible ($\varphi = 0$; fully-kinetic) and fully-reversible ($\varphi \rightarrow 1$; equilibrium) conditions. We parameterize the reversibility as a simple function of H_2 concentration by assuming Michaelis-Menten kinetics for each H-addition step:

$$\phi_n = 1 - \frac{[H_2]}{K_M + [H_2]} \quad [1]$$

where n represents the step number and K_M is the effective half-saturation constant for H_2 (assumed identical for steps 2–5). In our model, φ_1 is set at 1 (i.e., CO_2 uptake is fully reversible).

Under an assumption of steady-state concentrations of intermediates, all fluxes for the ^{12}CH isotopologues are dependent upon the methane formation rate (v_6, in e.g., mol $cell^{-1}$ s^{-1}) by:

$$v_n = \frac{v_6}{1-\phi_n}, \text{ and } w_n = \frac{\phi_n v_6}{1-\phi_n} \quad [2]$$

A series of continuity equations can be written for each ^{13}C-substituted isotopologue. For example:

$$\frac{d^{13}\mathbf{D}}{dt} = {}^{13}\alpha_3^+ \cdot v_3 \cdot {}^{13}r_{\mathbf{C}} - ({}^{13}\alpha_4^+ \cdot v_4 + {}^{13}\alpha_3^- \cdot w_3) \cdot {}^{13}r_{\mathbf{D}} + {}^{13}\alpha_4^- \cdot w_4 \cdot {}^{13}r_{\mathbf{E}}$$

Here, $^{13}\mathbf{D}$ is the abundance of ^{13}C-substituted isotopologues for the pool **D** (i.e., R-CH_2; fig. S4), and $^{13}r_{\mathbf{X}}$ is the isotopologue ratio of the pool **X** (where **X** = **A**, **B**, …, **F**), and $^{13}\alpha_n^+$ and $^{13}\alpha_n^-$ are the $^{13}C/^{12}C$ kinetic

isotope effects associated with the forward and backward reactions, respectively. There are a total of five continuity equations for pools $^{13}\mathbf{B}$, $^{13}\mathbf{C}$, $^{13}\mathbf{D}$, $^{13}\mathbf{E}$, and $^{13}\mathbf{F}$. Under an assumption of steady-state concentrations of intermediate species (i.e., $d^{13}\mathbf{X}/dt = 0$), we solve for the ratios of ^{13}C-containing to ^{12}C-containing isotopologues in the product methane (**F**; i.e., $^{13}CH_4/^{12}CH_4$) and in the intermediates (**B**, **C**, **D**, and **E**). The $^{13}C/^{12}C$ ratio of CO_2 (i.e., $r_\mathbf{A}$) is assigned.

For the deuterated isotopologues, the continuity equations account for both primary isotope effects (describing the rates at which C-D bonds are formed or broken relative to C-^{1}H bonds; fluxes shown vertically in fig. S4) and secondary isotope effects (describing the change in reaction rate resulting from D substitution at a site *adjacent* to that which is site of an ^{1}H-addition or abstraction reaction; fluxes shown horizontally in fig. S4). For example for reservoir **D**, the continuity equation for the D-substituted isotopologue (i.e., R-CH_2 or R-CHD) is:

$$\frac{d^2\mathbf{D}}{dt} = {}^2\alpha^+_{3\mathrm{p}} \cdot v_3 \cdot {}^2r_\mathbf{H} + {}^2\alpha^+_{3\mathrm{s}} \cdot v_3 \cdot {}^2r_\mathbf{C} - \left(\tfrac{1}{2} \cdot {}^2\alpha^-_{3\mathrm{s}} \cdot w_3 + \tfrac{1}{2} \cdot {}^2\alpha^-_{3\mathrm{p}} \cdot w_3 + {}^2\alpha^-_{4\mathrm{s}} \cdot v_4\right) \cdot {}^2r_\mathbf{D} + \tfrac{2}{3} \cdot {}^2\alpha^-_{4\mathrm{s}} \cdot w_4 \cdot {}^2r_\mathbf{E} \quad [3]$$

Here, $^2\alpha_{pn}$ and $^2\alpha_{sn}$ are primary and secondary deuterium isotope effects, and $^2r_\mathbf{X}$ are D-isotopologue ratios for reservoir **X**. $^2r_\mathrm{H}$ is the D/H ratio of hydrogen source (i.e., cellular water). The stoichiometric factor corresponds to the probability of a primary versus secondary isotope-sensitive reaction occurring (in this case, there is 2/3 chance of removing H from R-CH_2D). Again, there are five linear equations to be solved simultaneously. Conversion between isotopologue ratios and isotope ratios requires consideration of reaction stoichiometry. For example,

$${}^2r_\mathbf{D} = \frac{[\mathrm{R{=}CHD}]}{[\mathrm{R{=}CH_2}]} = 2\left(\frac{\mathrm{D}}{\mathrm{H}}\right)_{\mathrm{R{=}CH_2}} \quad [4]$$

Clumped isotopologue ratios (e.g., [R=^{13}CHD]/[R=$^{12}CH_2$]) can be solved for in a manner similar to that used for D-substituted isotopologues above.

For simplicity, primary (α_p) and secondary (α_s) kinetic isotope fractionation factors for the four H-addition steps are assumed to be identical at a given temperature (fractionation factors calculated for a model temperature of 20 °C are shown in table S3). The intrinsic (kinetic/forward) $^{13}C/^{12}C$ and D/H fractionation factors are estimated from *in vitro* and culture studies (*17*, *49–52*). The intrinsic ^{13}CD fractionation factor (γ, where $^{13D}\alpha = \gamma \cdot {}^{13}\alpha \cdot {}^2\alpha$) is taken to have the value required to generate a $\Delta^{13}CH_3D$ signature of either −1.3‰ or −3.5‰ under fully-kinetic conditions (main text and table S3). The $^{13}C/^{12}C$, D/H, and $^{13}CH_3D$ equilibrium isotope fractionation factors are based on experimental and/or theoretical calibrations (Fig. 2 and figs. S1 and S3) (*14*, *36*, *53*, *54*). The intrinsic fractionation factors for the reverse reactions (α^-, table S3) are constrained by the requirement for consistency among equilibrium (α_e), forward (α^+), and reverse reactions (i.e., $\alpha_{eq} = \alpha^-/\alpha^+$). We note that varying the secondary isotope effect (α_s, assumed to be 0.84 in either direction, for all steps) changes the curvature of the modeled microbial trajectories, but does not change the endmember $\varepsilon_{methane/water}$ values (which are set by the primary D/H isotope effect).

We initiated the model calculations at temperatures of 0, 20, and 40 °C. These temperatures bracket the range of known or inferred environmental temperatures at which the microbial methane samples we studied were generated (table S4). The predicted isotopic compositions for microbial methane generated between 0 and 40 °C are shown in Figs. 2 and 4.

Supplementary Text

Evaluation of alternative mechanisms for isotopic disequilibria in microbial methane

There are several potential alternative mechanisms for the observed isotopic disequilibria in microbial methane shown in Fig. 2. It is conceivable that these signals are due to mixing of multiple methane sources with differing $\delta^{13}C$ and δD values, as $\Delta^{13}CH_3D$ changes non-linearly upon mixing. The magnitude of non-linearity in the mixing depends on the difference in both $\delta^{13}C$ and δD values of the endmembers. It can be shown, using a Taylor-series expansion (*55*), that two-component mixing of endmembers (A & B) produces a mixture with a $\Delta^{13}CH_3D$ value of:

$$\Delta^{13}CH_3D_{mixture} \approx f_A[\Delta^{13}CH_3D]_A + (1 - f_A)[\Delta^{13}CH_3D]_B + f_A(1 - f_A)(\delta^{13}C_A - \delta^{13}C_B)(\delta D_A - \delta D_B) \quad [5]$$

where f_A represents the fractional contribution from endmember A. Accordingly, the observed ~6‰ negative bias in $\Delta^{13}CH_3D$ values (from that expected for equilibrium at 0–40 °C, Fig. 1) requires mixing of two methane sources with $\delta^{13}C$ and δD values that differ by ±60‰ and ∓400‰, respectively; gases with these isotopic compositions are unlikely to co-occur in the environments we studied (*7*).

Alternatively, under a commonly-used classification based on $\delta^{13}C$ and δD values (*13*), methane from these sites could be interpreted as derived from methyl-type fermentation (Fig. 1). If so, the low $\Delta^{13}CD$ values could be inherited from those of the C–H bonds in methyl groups of the organic substrate(s). However, theoretical calculations predict consistent $\Delta^{13}CD$ clumping effects of +6.2 ± 0.3‰ at 25 °C for the C-H bond of simple organic compounds (table S6), which is not significantly different from the equilibrium value for $\Delta^{13}CH_3D$ at 25 °C (+6.4‰). Thus, inheritance of equilibrium $\Delta^{13}CD$ values from organic precursors during methyl-type fermentation does not explain the observed disequilibrium $\Delta^{13}CH_3D$ signatures. While inheritance of kinetically-influenced $\Delta^{13}CD$ values from organic precursors is possible, the $\Delta^{13}CD$ values of acetate and other methyl-bearing methanogenic substrates are not currently known.

Furthermore, oxidation of methane can also be ruled out because the substantial deuterium-enrichment associated with methane oxidation (*13*) is not observed in the samples we studied.

The equilibrium hydrogen-isotopic fractionation between water and methane

We compiled previously-published equilibrium hydrogen-isotopic fractionation factors calibrated at various temperatures, either experimentally or theoretically, for the system $CH_4(g)$-$H_2(g)$-$H_2O(g)$-$H_2O(l)$. The $H_2O(l)/H_2(g)$ fractionation factor is very large (α is ~4 at room temperature), and calibrations diverge substantially at lower temperatures (<100 °C, fig. S3); this is the main source of uncertainty in estimates of $CH_4(g)/H_2O(l)$ equilibrium D/H fractionation, which is derived by combination of $H_2O(l)/H_2(g)$, $H_2(g)/H_2O(g)$, and $CH_4(g)/H_2(g)$ calibration curves. We used the Cerrai et al. (*53*) calibration for $H_2O(l)/H_2(g)$ in the calculation of $\varepsilon_{methane/water}$ of the equilibrium endmember of our model for isotope effects accompanying microbial methanogenesis (see model description) because amongst the published calibrations, this is likely most accurate at lower temperatures (*36*, *56*, *57*). The uncertainty in calibration, as well as salt and pressure effects (*58*), could explain small apparent offsets from the equilibrium line (Fig. 2) for some samples of thermogenic methane.

Field site descriptions and sampling methods

Bovine rumen, State College, Pennsylvania, USA. The bovine rumen gas samples obtained for this study were collected from cannulated, lactating Holstein dairy cows at The Pennsylvania State University using methods described previously (*59*). The samples were stored at room temperature in glass serum vials stoppered with blue butyl septa. Bovine rumen fluid was also sampled for water isotope analysis (table S4). The fluid was centrifuged to remove large particulate material, filtered with a 0.2 µm filter, and distilled to remove dissolved organic matter prior to isotope-ratio analysis. We note that the rumen fluid and gas samples were not taken from the same animal at the same time. However, the temporal variation of δD of tap water in the U.S. is expected to be small (generally <10‰ in any particular region over multiple seasons) (*60*).

Northern Cascadia Margin. Gas samples were collected from gas voids and hydrates in sediment cores drilled during IODP (Integrated Ocean Drilling Program) Expedition 311 (*61*). These gases were interpreted to be dominantly microbial based on isotopic and compositional analyses (e.g., $C_1/C_2 > 1000$) (*3*). The gas samples were subsampled for previous analyses, and have remained in archive since. Samples were contained either in serum vials sealed with blue butyl stoppers, or in Vacutainers® (Becton Dickinson) sealed with orange septa and an additional silicone plug (in table S1, these are denoted "SB" or "Vac", respectively); these methods are standard IODP procedures. The sample ID's for the samples from the Northern Cascadia Margin listed in table S1 are the same as those reported in Pohlman et al. (*3*).

Powder River Basin, Wyoming, USA. The Powder River Basin is a major source of coal and coalbed methane. Gas samples were collected from multiple gas wells producing from the methane-rich Wall and Cook coal seams using a wellhead gas sampler and IsoTubes (from Isotech Laboratories, Champaign, Illinois, USA). Water samples were collected concurrently from the same wells, filtered through 0.45 µm nylon filters, transported to the lab on ice in deionized water-washed glass bottles with no headspace, and kept at 4 ^{o}C prior to analysis.

Atlantic White Cedar swamp, Cape Cod, Massachusetts, USA. Atlantic White Cedar swamps are wetlands found throughout the coastal northeastern United States (*62*). We collected gases and water from a swamp ("Swamp Y", approximate coordinates 41°31'38.2"N, 70°39'15.5"W) on the campus of the Marine Biological Lab (MBL) in Woods Hole, MA in May 2014. Gases were collected by trapping the bubbles released when sediment on the bottom of the swamp was gently disturbed. The collected gases were transferred via syringes to serum vials (either pre-evacuated or pre-filled with NaCl brine that was displaced to make room for the gas sample) sealed with blue butyl septa, and stored at room temperature until analysis. One sample ("SwampY-5", table S1) was subsampled and analyzed 3 days after sample collection, and again 3 weeks later. The measured $\Delta^{13}CH_3D$ values were indistinguishable within the precision of the measurements (0.36 ± 0.34‰ and 0.27 ± 0.52‰, respectively).

Upper Mystic Lake, Arlington, Massachusetts, USA. Upper Mystic Lake is a freshwater lake in the Boston metropolitan area. Ebullition of methane from this lake has been previously documented (*34*, *63*). We collected gas bubbles using inverted funnel-shaped bubble traps [modified from an inverted-funnel design described previously (*34*, *64*)] deployed ~2 m above the lake floor (~18 m water depth) using a custom rope and buoy structure. The deep deployment depth was chosen to minimize dissolution and/or oxidation of bubbles during their transit from the sediment to the lake surface. The collected gases were transferred via syringes to serum vials (either pre-evacuated or pre-filled with deionized water that was

displaced to make room for the gas sample) sealed with blue butyl septa, fixed with either saturated NaCl solution or 1 M NaOH, and stored at either 4 °C or room temperature until analysis. The water sample from Upper Mystic Lake listed in table S4 was collected in September 2014.

Lower Mystic Lake, Arlington, Massachusetts, USA. Lower Mystic Lake (elevation 1 m above sea level, maximum depth 24 m) is a meromictic glacial kettle lake. The sample of methane reported in table S1 was extracted from water we collected from 20 m water depth (mbll, meters below lake level) in August 2014. The water sample was transferred into a 2 L media bottle, taking care to minimize bubbles, immediately stoppered with a black rubber septum (Glasgerätebau Ochs, Germany), and transported to the laboratory. A headspace was created using helium, and the sample was then stored at 4 °C until extraction and analysis. The concentration of dissolved methane at 20 mbll was determined to be 4.2 mM (±5%). Field measurements indicated that the water at 20 mbll was oxygen-depleted and had elevated conductivity relative to surface water. The water sample listed in table S4 was collected from 18 mbll, which is below the chemocline.

The Cedars, Cazadero, California, USA. Samples of bubbling gases were collected in June 2013 and July 2014 from sites in The Cedars as described in Morrill et al. (*29*); the sites studied here were Barnes Spring Complex (BSC), and Nipple Spring (NS). Gas samples were collected in inverted-bucket traps positioned over seeps, and collected gases were transferred to serum bottles stoppered with blue butyl rubber septa. Samples were fixed with $HgCl_2$ or HCl to prevent microbial alteration of the methane.

Coast Range Ophiolite Microbial Observatory, Lower Lake, California, USA. The Coast Range Ophiolite Microbial Observatory, located at the McLaughlin Natural Reserve (UC Davis), was established in 2011 with the completion of eight ultramafic-hosted groundwater monitoring wells drilled using a mud-free technique (*30*, *65*). Water was sampled from well "N-08A" in December 2013 using a bladder pump into 1–2 L bottles, stoppered immediately as described above for the Lower Mystic Lake sample, transported to the laboratory, and stored at 4 °C until extraction and analysis. We also collected water in July 2014 from an electrically-pumped non-potable groundwater well in the Core Shed area ("CSWold", approximate coordinates 38°51'42.53"N, 122°24'53.05"W). For this sample, dissolved gases were extracted on-site via equilibration with a helium headspace and stored in a stoppered serum vial fixed with 0.5 ml 1 M HCl. The water sample for which the δD_{water} value is reported in table S4 was collected from CSWold in December 2013. The range of H_2 concentrations reported in table S4 from CROMO are minimum and maximum values of [H_2] observed over multiple sampling trips during a long-term (~3 years) sampling campaign.

Kidd Creek Mine, Timmins, Ontario, Canada. In subsurface mines in the Canadian Shield, exploration boreholes intersecting extensive fracture networks release waters rich in reduced gases (H_2, CH_4, C_{2+}) and noble gases, which exsolve upon depressurization. Sampling and characterization of fracture fluids from Kidd Creek have been described in previous studies (*4*, *5*, *31*, *66*, *67*). We analyzed methane sampled from boreholes at the 7850'- and 9500'-levels (table S1). These samples were taken between 2007 and 2014, and stored in glass serum vials stoppered with blue butyl rubber septa. The $\delta^{13}C$ values of these gases were previously measured by GC-IRMS at the University of Toronto. No evidence of any effects of long-term storage on the $\delta^{13}C$ of methane in these samples has been observed; the average difference between $\delta^{13}C$ determined via TILDAS compared to GC-IRMS was 0.09 ± 0.60‰ (1*s*, $n = 9$), and shows no correlation with the length of time the sample had been stored.

Guaymas Basin hydrothermal system (Rebecca's Roost vent), Gulf of California. Guaymas Basin in the Gulf of California hosts an active sediment-hosted mid-ocean ridge hydrothermal system.(*68–70*). We analyzed methane from a fluid sample taken from a 299 °C vent fluid emanating from Rebecca's Roost, a flange-like vent structure. The sample was taken in 2008 using a isobaric gas-tight sampler (table S1) and poisoned with mercuric chloride (*71*). Fluid properties and geochemical data associated with this sample have been previously published (*22*). We assumed a value of +4 ± 2‰ for the δD_{water} of the vent fluid based on previous observations of Guaymas Basin hydrothermal vent fluid waters (*72*).

Northern Appalachian Basin, Central Pennsylvania, USA. Gases were sampled from gas wells producing from the Marcellus Formation (Middle Devonian) and Utica Formation (Upper Ordovician) in central Pennsylvania using standard wellhead sampling techniques. Gases produced from these geologic units are dry (<5% $C_{2+}/\Sigma C_{1-5}$) thermogenic gases of high thermal maturity (*1*, *16*). The C_2/C_1 ratios of the gas samples from the Marcellus and Utica Shales we analyzed were <100 (table S4), which is within the range expected for thermogenic gases (*73*, *74*).

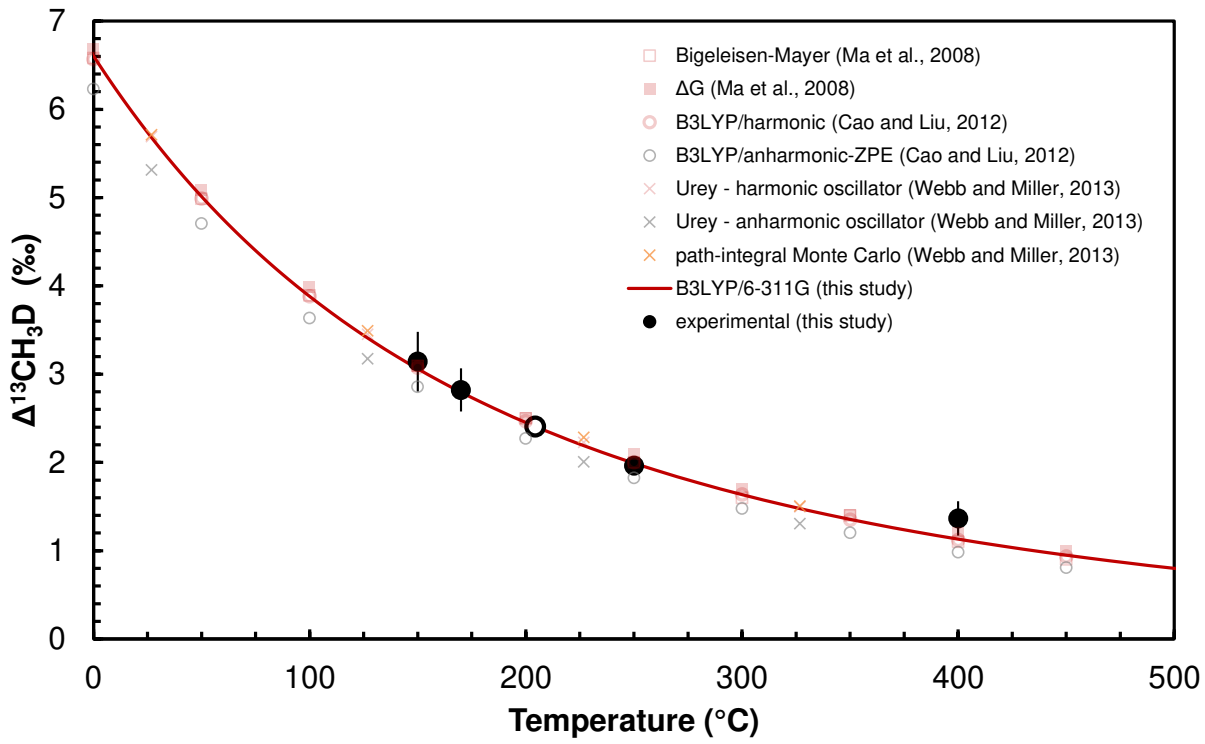

Fig. S1. Experimental calibration of the $\Delta^{13}CH_3D$ thermometer. Filled circles represent the mean $\Delta^{13}CH_3D$ of gases heated at that temperature, and error bars represent 95% confidence intervals calculated from a normal distribution (for the 150 °C sample, error bars represent the 95% confidence interval on the measurement cycles in a single analysis calculated from a *t*-distribution). For the 250 °C point, the error bars are smaller than the symbol. The open circle represents our reference gas, AL1. The equilibrium curve (red line) was calculated following conventional equilibrium isotope fractionation theory under the harmonic oscillator assumption (*75*); frequencies were calculated at the B3LYP level of theory using the 6-311G basis set as implemented in Gaussian 03 (*76*). For comparison, results from published computational studies (*44–46*) are also plotted.

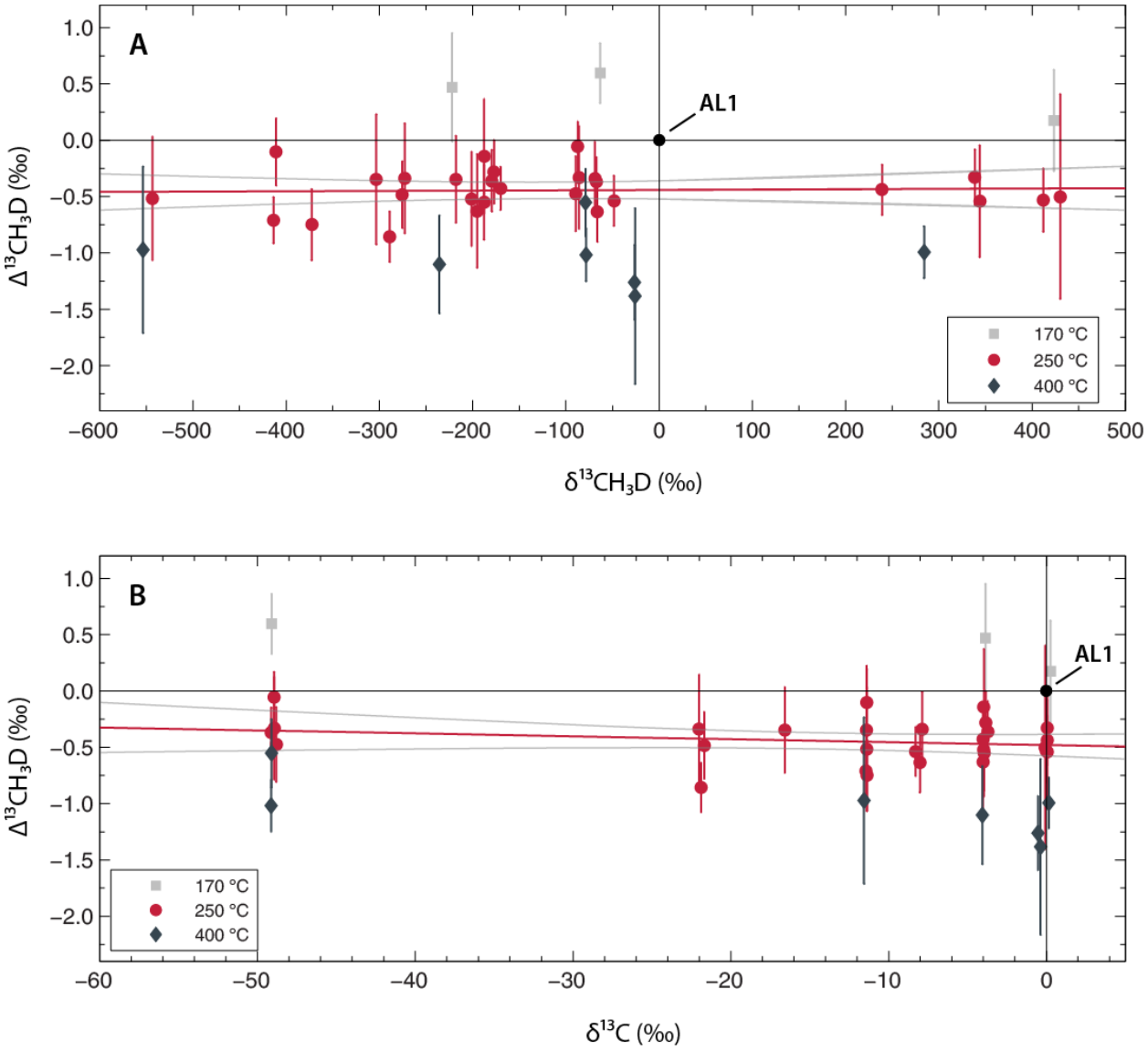

Fig. S2. Measurements of methane heated over catalyst at various temperatures. Solid red lines represent unweighted linear least squares regressions through gases equilibrated at 250 °C, and gray lines denote the 95% confidence band. Error bars represent 95% confidence intervals on multiple measurement cycles of a single analysis. Isotopic ratios are shown relative to our reference gas, AL1. Results indicate no significant correlation between $\Delta^{13}CH_3D$ and (**A**) $\delta^{13}CH_3D$ over an 800‰ range (the variation in $\delta^{13}CH_3D$ is driven mainly by differences in δD); and (**B**) $\delta^{13}C$ over a 48‰ range.

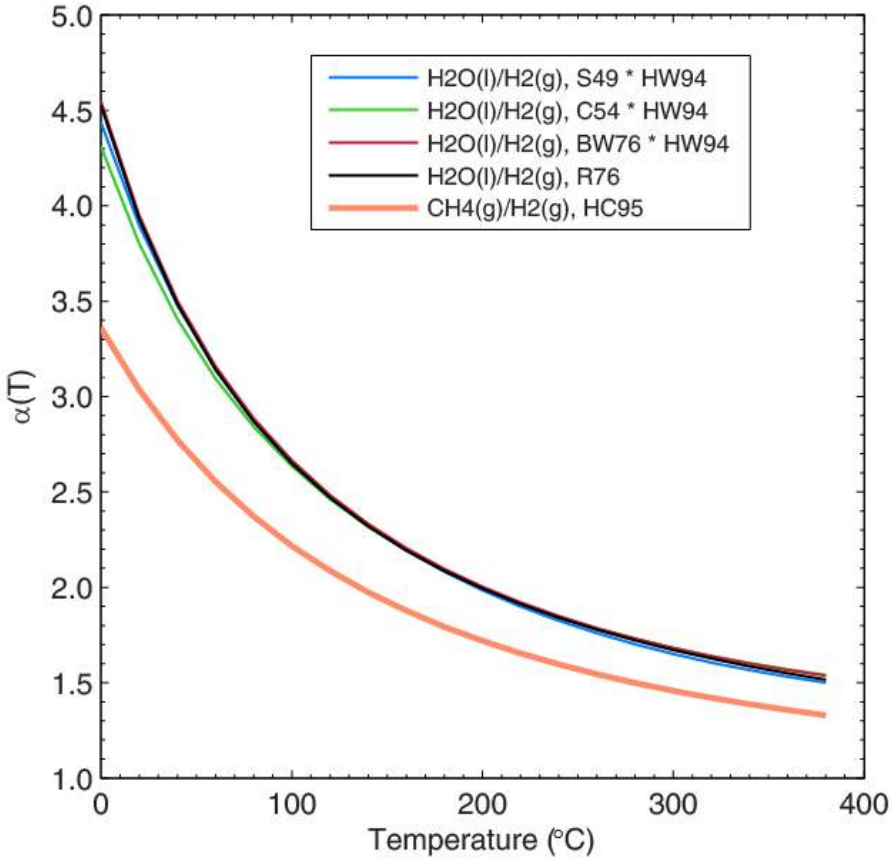

Fig. S3. Equilibrium hydrogen isotopic fractionation factors compiled from experimental and theoretical calibrations. When appropriate, calibrations for $H_2O(g)/H_2(g)$ have been converted using the $H_2O(l)/H_2O(g)$ calibration from Horita and Wesolowski (*77*) to derive $H_2O(l)/H_2(g)$ calibrations. HW94, Horita and Wesolowski (*77*); S49, Suess (*57*); C54, Cerrai et al. (*53*); BW76, Bardo and Wolfsberg (*78*); R76, Rolston et al. (*56*); HC95, Horibe and Craig (*36*). For any temperature, the $CH_4(g)/H_2O(l)$ equilibrium composition is the ratio of the $CH_4(g)/H_2(g)$ line (HC95) to a $H_2O(l)/H_2(g)$ line.

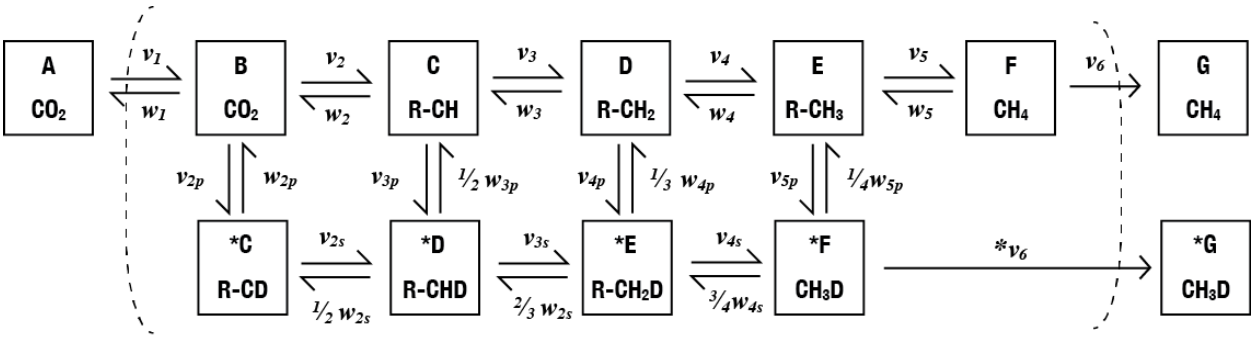

$w_1/v_1 = 1$; $w_n/v_n = 1\text{-}[H_2]/(K_m+[H_2])$ (for n=2, 3, 4, and 5)

$v_{np} = {}^2\alpha_p{}^+ \, v_{np} \, (D/H)_{H2O}$; $w_{np} = {}^2\alpha_p{}^- \, w_{np}$

$v_{ns} = {}^2\alpha_s \, v_{ns}$; $w_{ns} = {}^2\alpha_s w_{ns}$

Fig. S4. Schematic of the model of deuterium substitution during microbial methanogenesis from CO_2. Boxes represent pools of cellular carbon involved in the methanogenic pathway, and the asterisk represents a compound containing a deuterium substitution. Forward flows are represented by *v*, and backwards flows are represented by *w*. The model setup is similar in concept to previously published models for microbial sulfate reduction (*25*, *79*, *80*).

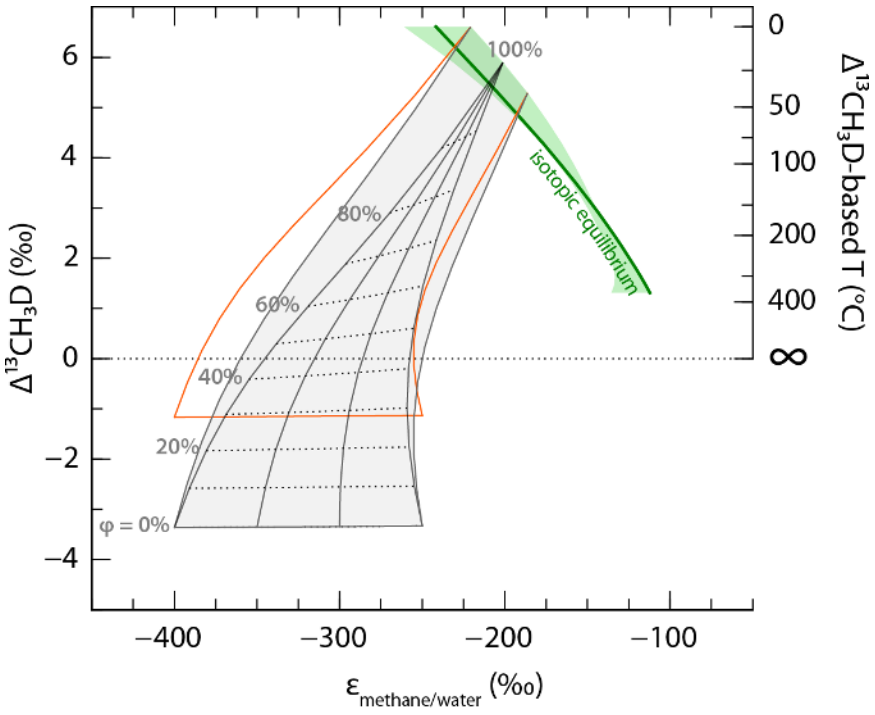

Fig. S5. Dependence of the modeled isotopic composition of microbial methane on the degree of reversibility and isotope fractionation factors. Orange and gray fields represent model output assuming a kinetic endmembers of −1.3‰ and −3.5‰, respectively (table S3). Inner solid gray lines represent model trajectories for 20 °C assuming different values for the D/H primary intrinsic isotope effect (table S3). Subhorizontal tie lines connect points of equal reversibility (φ). Outer solid lines represent bounding model trajectories calculated for 0 and 40 °C.

Table S1. Results of isotopic measurements of natural samples of methane. Uncertainties reported are 95% confidence intervals over all measurement cycles for a single analysis. Values for $\delta^{13}C$, δD, and $\Delta^{13}CH_3D$ are reported relative to PDB, SMOW, and the stochastic distribution, respectively. Samples for which $\Delta^{13}CH_3D \leq 0‰$ have no corresponding thermodynamically-allowed apparent equilibrium temperature, and are noted as anti-clumped (a.c.).

Sample Set	Sample Name	$\delta^{13}C$ (‰)		δD (‰)		$\Delta^{13}CH_3D$ (‰)		T_{13D} (°C)	
Bovine Rumen	Sally-1*	**-52.81**	± 0.04 ‰	**-342.56**	± 0.04 ‰	**1.46**	± 0.71 ‰	**330**	+190/–101 °C
	Sally-2-5*	**-54.15**	± 0.07 ‰	**-347.25**	± 0.07 ‰	**0.76**	± 0.49 ‰	**515**	+309/–144 °C
NCM	311-1325B-19X-4 (145-146) / Void, SB	**-68.50**	± 0.10 ‰	**-189.48**	± 0.10 ‰	**5.74**	± 0.49 ‰	**25**	+16/–15 °C
	311-1325C-6X-4 (17-18) / Void, SB	**-67.63**	± 0.07 ‰	**-188.40**	± 0.07 ‰	**5.22**	± 0.29 ‰	**42**	+11/–10 °C
	311-1328E-2X-CC (0-10) / Hyd, SB	**-63.14**	± 0.04 ‰	**-193.26**	± 0.04 ‰	**6.14**	± 0.21 ‰	**13**	+6/–6 °C
	311-1328E-2X-CC (0-10) / Hyd, Vac	**-61.63**	± 0.08 ‰	**-191.14**	± 0.08 ‰	**6.17**	± 0.34 ‰	**12**	+10/–9 °C
PRB	DR_15W-17-08-41	**-59.74**	± 0.08 ‰	**-292.75**	± 0.12 ‰	**5.42**	± 0.34 ‰	**35**	+12/–11 °C
	DR_3CA34	**-62.03**	± 0.10 ‰	**-290.80**	± 0.10 ‰	**4.95**	± 0.63 ‰	**52**	+26/–22 °C
	DR_Visborg_13W-17-08-41	**-58.58**	± 0.10 ‰	**-293.89**	± 0.10 ‰	**5.19**	± 0.43 ‰	**44**	+16/–15 °C
Swamp Y	SwampY-1	**-59.72**	± 0.06 ‰	**-322.17**	± 0.06 ‰	**0.47**	± 0.33 ‰	**660**	+318/–159 °C
	SwampY-2	**-59.25**	± 0.06 ‰	**-324.27**	± 0.06 ‰	**1.00**	± 0.55 ‰	**435**	+238/–121 °C
	SwampY-5†	**-59.70**	± 0.32 ‰	**-330.14**	± 0.21 ‰	**0.32**	± 0.10 ‰	**775**	+100/–78 °C
UML	UML 06/19/2014	**-70.96**	± 0.10 ‰	**-264.97**	± 0.10 ‰	**3.22**	± 0.43 ‰	**139**	+32/–26 °C
	UML 07/29/2014	**-70.99**	± 0.16 ‰	**-268.93**	± 0.16 ‰	**3.13**	± 0.67 ‰	**145**	+54/–41 °C
LML	LML-20m	**-65.47**	± 0.07 ‰	**-289.81**	± 0.07 ‰	**0.98**	± 0.35 ‰	**440**	+133/–87 °C
The Cedars	The Cedars NS, 2013 June	**-67.97**	± 0.12 ‰	**-333.06**	± 0.07 ‰	**-2.43**	± 0.62 ‰	a.c.	
	The Cedars BSC, 2013 June	**-63.81**	± 0.21 ‰	**-341.98**	± 0.16 ‰	**-3.36**	± 1.42 ‰	a.c.	
	The Cedars BSC, 2014 July	**-64.39**	± 0.05 ‰	**-341.48**	± 0.05 ‰	**-2.93**	± 0.24 ‰	a.c.	
Kidd Creek	14.06.2012.KC.L9500_BHY13762_Gas D	**-32.66**	± 0.07 ‰	**-420.74**	± 0.07 ‰	**4.38**	± 0.80 ‰	**76**	+41/–32 °C
	29.11.2012.KC.L9500_BH2_Gas C	**-32.28**	± 0.07 ‰	**-419.74**	± 0.06 ‰	**4.07**	± 0.29 ‰	**90**	+15/–14 °C
	KC_12.02.2008_7850L_BH12299(E)	**-39.11**	± 0.11 ‰	**-397.33**	± 0.05 ‰	**4.51**	± 0.25 ‰	**70**	+11/–10 °C
	KC_12.01.2010_7850L_BH12299(F)	**-39.73**	± 0.06 ‰	**-397.39**	± 0.06 ‰	**4.34**	± 0.52 ‰	**78**	+26/–22 °C
	KC_01.03.2012_7850L_BH12299(F)‡	**-40.19**	± 0.05 ‰	**-394.98**	± 0.03 ‰	**4.11**	± 0.37 ‰	**89**	+19/–17 °C
	02.04.2014_KC_7850L_BH12299(C)	**-39.72**	± 0.04 ‰	**-390.12**	± 0.03 ‰	**4.47**	± 0.22 ‰	**72**	+10/–9 °C
	02.04.2014_KC_7850L_BH12299(D)	**-39.72**	± 0.06 ‰	**-390.12**	± 0.06 ‰	**4.07**	± 0.26 ‰	**90**	+13/–12 °C
	KC_27.08.2007_7850L_BH12287A(C)	**-40.64**	± 0.04 ‰	**-386.48**	± 0.05 ‰	**4.36**	± 0.22 ‰	**77**	+10/–10 °C
	KC_20.06.2008_7850L_BH12287A(D)	**-40.25**	± 0.08 ‰	**-395.07**	± 0.05 ‰	**4.23**	± 0.30 ‰	**83**	+15/–13 °C
	KC_20.09.2013_7850L_BH12287A(B)	**-41.44**	± 0.06 ‰	**-388.32**	± 0.06 ‰	**4.87**	± 0.32 ‰	**56**	+13/–12 °C
NAB	Marcellus Fm.	**-36.18**	± 0.09 ‰	**-157.60**	± 0.07 ‰	**3.10**	± 0.33 ‰	**147**	+25/–22 °C
	Utica Fm.	**-25.70**	± 0.08 ‰	**-153.10**	± 0.08 ‰	**2.93**	± 0.36 ‰	**160**	+29/–25 °C
Guaymas	Rebecca's Roost 4462-IGT4, VT1	**-43.96**	± 0.18 ‰	**-106.24**	± 0.16 ‰	**1.48**	± 0.67 ‰	**326**	+170/–95 °C
CROMO	CROMO-CSWold	**-26.98**	± 0.07 ‰	**-169.56**	± 0.07 ‰	**4.39**	± 0.29 ‰	**76**	+14/–12 °C
	CROMO-N08-A.1	**-26.39**	± 0.07 ‰	**-157.53**	± 0.06 ‰	**5.24**	± 0.31 ‰	**42**	+11/–10 °C
	CROMO-N08-A.2	**-26.55**	± 0.12 ‰	**-157.50**	± 0.13 ‰	**4.97**	± 0.44 ‰	**52**	+18/–16 °C

Abbreviations: NCM, Northern Cascadia Margin; PRB, Powder River Basin; Swamp Y, Atlantic White Cedar Swamp; UML, Upper Mystic Lake; LML, Lower Mystic Lake; NAB, Northern Appalachian Basin; CROMO, Coast Range Ophiolite Microbial Observatory.

* Purified sample was measured twice. The uncertainties reported for these samples are 95% confidence intervals calculated from the data for each measurement (with σ taken as the larger of 1*s* or 0.3‰, which is typical analytical reproducibility) assuming the measurements follow a normal distribution.

† Sample was subsampled, purified and analyzed twice (3 weeks apart) as described in the *SI Text*. The uncertainties reported for this sample are 2 s.e.m. (standard error of the mean) of the replicate measurements ($n = 2$).

‡ Sample was subsampled, purified and analyzed three times over a period of >3 months. The uncertainties reported for this sample are 2 s.e.m. of the replicate measurements ($n = 3$).

Table S2. Results of isotopic measurements of methane produced experimentally by cultures of methanogens. Each line represents a separate bottle incubation of an axenic strain of methanogens. Uncertainties reported are 95% confidence intervals over all measurement cycles for a single analysis. Values for $\delta^{13}C$, δD, and $\Delta^{13}CH_3D$ are reported relative to PDB, SMOW, and the stochastic distribution, respectively. Samples for which $\Delta^{13}CH_3D \leq 0‰$ have no corresponding thermodynamically-allowed apparent equilibrium temperature, and are noted as anti-clumped (a.c.).

Culture	growth T*	$\delta^{13}C$ (‰)		δD (‰)		$\Delta^{13}CH_3D$ (‰)		T_{13D} (°C)	
Methanocaldococcus bathoardescens	85 °C	**-12.58**	± 0.07 ‰	**-419.23**	± 0.07 ‰	**1.03**	± 0.45 ‰	**426**	+170/–100 °C
Methanocaldococcus jannaschii	80 °C	**-18.79**	± 0.03 ‰	**-416.90**	± 0.05 ‰	**2.29**	± 0.23 ‰	**216**	+25/–22 °C
Methanothermococcus thermolithotrophicus	60 °C	**-17.05**	± 0.05 ‰	**-409.84**	± 0.05 ‰	**0.54**	± 0.28 ‰	**620**	+214/–126 °C
Methanothermococcus thermolithotrophicus	40 °C	**-16.47**	± 0.04 ‰	**-427.76**	± 0.04 ‰	**1.38**	± 0.34 ‰	**345**	+79/–58 °C
Methanosarcina barkeri	ambient	**-59.90**	± 0.05 ‰	**-418.40**	± 0.05 ‰	**-1.34**	± 0.22 ‰	a.c.	
Methanosarcina barkeri	ambient	**-50.30**	± 0.07 ‰	**-422.67**	± 0.07 ‰	**-1.08**	± 0.63 ‰	a.c.	

* Uncertainty on measured growth temperatures is estimated at ±5 °C. Temperatures were not monitored throughout the *M. barkeri* incubations but are estimated at 25 ± 10 °C.

Table S3. Isotope fractionation factors (input parameters) used in model calculations for microbial methane generated at 20 °C. A detailed description of the model setup and explanation of choices of fractionation factors is given in *Materials and Methods*.

	forward	backward	equilibrium
$^{13}C/^{12}C$ isotope effect ($^{13}\alpha$)	0.9600*	0.9771†	0.9824‡
D/H primary isotope effect ($^{2}\alpha_{p}$)	0.600 to 0.750§	0.751 to 0.939†	0.7989‖
D/H secondary isotope effect ($^{2}\alpha_{s}$)	0.8400¶	0.8400¶	1.0000†
^{13}C-D clumped isotope effect (γ)	0.9987 or 0.9965**	0.9928 or 0.9907†	1.0059††

* From Scheller et al. (*52*) for the reduction of methyl-coenzyme M.

†Internally-consistent value.

‡ From Horita (*54*), who determined $^{13}\alpha_{CH4/CO2}$ = 0.932 at 20 °C; this reported value is equal to 0.9824 taken to the power of 4.

§ Free parameter. The range of values used here are similar to those reported for *in vitro* studies of methyl-coenzyme M reductase (0.63 to 1.0) (*52*) and from experimental cultures of methanogens (0.70 to 0.86) (*17*).

‖ From the value given by Horibe and Craig (*36*) for the equilibrium D/H fractionation factor between H_2O(l) and CH_4(g) at 20 °C.

¶ From Scheller et al. (*52*) for the reduction of methyl-CoM.

** To fit the lowest $\Delta^{13}CH_3D$ values we have observed in methanogen culture experiments (0.9987, corresponding to $\Delta^{13}CH_3D = -1.3‰$, table S2) or in nature (0.9965, corresponding to $\Delta^{13}CH_3D = -3.5‰$, table S1). Calculations for the fields shown in Figs. 2 and 4 use the latter values. See *Materials and Methods* for explanation of choice, and fig. S5 for comparison of model results using the two different values.

‡‡Computed equilibrium $\Delta^{13}CH_3D$ value at 20 °C (fig. S1).

Table S4. Methane/ethane ratio, hydrogen isotopic composition of water, current environmental temperatures, and concentration of dissolved H_2 for sites studied. References are provided for previously-published descriptions of the field site; n.d., not determined.

Location	C_1/C_2 ratio‖	δD_{water} (‰)¶		T (°C)**		$[H_2]$	Notes / Data Sources
Bovine rumen, State College, Pennsylvania, USA	n.d.	**-32**	± 10	**39**	± 2	*0.1–50 μM*	this study*,‡, (*81*)
Northern Cascadia Margin sediments	>1000	***+5***	*± 10*	**3–17**		*2–60 nM*	[1]
Powder River Basin, Wyoming, USA	>1000	**-136**	± 5	**18**	± 2	n.d.	this study§
Atlantic White Cedar swamp, Cape Cod, Massachusetts, USA	n.d.	**-21**	± 10	***16***	*± 5*	n.d.	this study‡
Upper Mystic Lake, Massachusetts, USA	n.d.	**-39**	± 10	**4**	± 2	n.d.	this study‡
Lower Mystic Lake, Massachusetts, USA	>1000	**-41**	± 10	**6**	± 2	n.d.	this study‡
The Cedars, California, USA	>350	***-37***	*± 10*	***17***	*± 1*	*120, 310 μM*	[2]
Coast Range Ophiolite Microbial Observatory, California, USA	>350	**-33**	± 10	**16**	± 4	60–130 nM	this study†,‡
Kidd Creek Mine, Timmins, Ontario, Canada	5.9–14	**-34**	± 6	**30**	± 2	*0.8–8 mM*	[3]
Guaymas Basin hydrothermal field (Rebecca's Roost vent)	140	***+4***	*± 2*	**299**	± 5	3.3 mM	(*22*, *72*)
Marcellus Fm., central Pennsylvania, USA	45	***-44***	*± 10*	**51**	± 10	n.d.	[4]
Utica Fm., central Pennsylvania, USA	84	***-40***	*± 15*	**93**	± 10	n.d.	[5]

* Concentrations of H_2 were determined using gas chromatography with thermal conductivity detection at MIT. Analytical reproducibility is typically ±5%.

† Concentrations of H_2 were determined using a reduced gas analyzer gas chromatograph at NASA Ames (*65*).

‡ The δD_{water} values were measured at the Boston University Stable Isotope Laboratory using high-temperature conversion gas chromatography isotope-ratio mass spectrometry. External reproducibility on replicate analyses of samples was ± 1–3‰ (1*s*, *n* = 3–4), with the exception of cow rumen fluid (±8‰, 1*s*).

§ The δD_{water} values were measured at the University of Arizona Environmental Geochemistry Laboratory via isotope-ratio mass spectrometry.

‖ Unless otherwise indicated, the C_1/C_2 ratio (i.e., the ratio of the concentration of methane to that of ethane in a gas sample) was determined using gas chromatography with flame-ionization detection at MIT.

¶ The δD_{water} values are reported with respect to the VSMOW scale.

#** At some sites ambient temperatures were not directly measured (*in italics*) and therefore were estimated; reasonable uncertainties on those estimates are given. At all other sites temperatures were measured in-situ.

[1] For the Northern Cascadia Margin samples, an average D/H ratio of marine sediment porewater [+5‰ (*82*)] is assumed. The natural variability of ±10‰ is taken as the uncertainty of this estimate. Downhole temperature measurements from Expedition 311 have been reported (*83*). Concentrations of H_2 were assumed to be within the range of 2–60 nM, which is typical of marine sediments (*84*). The C_1/C_2 data are from Pohlman et al. (*3*).

[2] The $[H_2]$, δD_{water} and temperature data are from Morrill et al. (*29*). An uncertainty of ±10‰ is applied to δD_{water} to account for potential interannual variability. Dissolved $[H_2]$ for estimated from the H_2 concentration in the gas phase assuming equilibrium between gas bubbles and water at atmospheric pressure.

[3] Dissolved $[H_2]$ for Kidd Creek fluids was estimated using gas/water flow rate data from Holland et al. (*31*) and gas-phase H_2 concentrations from Sherwood Lollar et al. (*4*), and assuming that all dissolved H_2 had completely partitioned into the gas phase prior to sampling. The C_1/C_2 data are from Sherwood Lollar et al. (*5*).

[4] The δD_{water} values for formation water from the Marcellus Fm. in Pennsylvania are estimated from Rowan et al. (*85*). Uncertainty on reservoir temperature is estimated at ±10 °C.

[5] The δD_{water} values for formation water from the Utica Fm. are estimated using data for Appalachian Basin brines from pre-Middle Devonian units presented in Warner et al. (*86*). Uncertainty on reservoir temperature is estimated at ±10 °C.

Table S5. Results of isotopic measurements of methane in samples of natural gas standards NGS-1 and NGS-3. Uncertainties reported are 95% confidence intervals over all measurement cycles for a single analysis as described in *Methods*. Values for $\delta^{13}C$, δD, and $\Delta^{13}CH_3D$ are reported relative to PDB, SMOW, and the stochastic distribution, respectively.

Sample Name	$\delta^{13}C$ (‰)		δD (‰)		$\Delta^{13}CH_3D$ (‰)		T_{13D} (°C)	
NGS-1	**-28.73**	± 0.05 ‰	**-137.47**	± 0.05 ‰	**2.61**	± 0.29 ‰	**186**	+28/–24 °C
	-28.79	± 0.07 ‰	**-137.69**	± 0.07 ‰	**2.53**	± 0.29 ‰	**193**	+29/–25 °C
	-28.91	± 0.05 ‰	**-138.07**	± 0.05 ‰	**2.62**	± 0.24 ‰	**185**	+22/–19 °C
NGS-3	**-72.82**	± 0.06 ‰	**-176.09**	± 0.06 ‰	**5.08**	± 0.26 ‰	**48**	+10/–9 °C
	-72.71	± 0.05 ‰	**-175.82**	± 0.05 ‰	**5.18**	± 0.26 ‰	**44**	+10/–9 °C
NGS-3 + 150ml air *	**-72.99**	± 0.06 ‰	**-176.21**	± 0.06 ‰	**5.14**	± 0.49 ‰	**45**	+19/–17 °C

* This sample was a subsample of NGS-3 that was intentionally-contaminated with 150 ml of air, to check for artifacts introduced from sample preparation and analysis of samples containing large quantities of air. No significant difference was found compared to subsamples of NGS-3 that were not contaminated with air.

Table S6. Partition function ratios (β-factors) for simple organic compounds calculated at 25 °C. Partition function ratios were calculated using the method of Bigeleisen and Mayer (*75*). Vibrational frequencies were calculated using the Hartree-Fock method with the 6-31G* basis set. The partition function ratios listed below have been corrected with symmetry factors to account for changes in symmetry upon isotope substitution (*75*, *87*). The average Δ^{13}CD value calculated for methanol, formaldehyde, formate, methanethiol, and acetate is +6.2 ± 0.3‰ (1*s*).

Species	Formula*	$^{13}C/^{12}C$	D/H	$^{13}CD/^{12}CH$	Δ^{13}CD (‰)
Methane	C**H**$_4$	0.123	2.647	2.777	6.4
Methanol	C**H**$_3$OH	0.150	2.812	2.968	6.3
Formaldehyde	C**H**$_2$O	0.165	2.591	2.763	6.7
Formate	**H**COOH	0.200	2.834	3.040	5.9
Methanethiol	C**H**$_3$SH	0.128	2.759	2.893	6.2
Acetate	C**H**$_3$COOH	0.147	2.775	2.927	6.0

* D/H and $^{13}CD/^{12}CH$ β-factors were calculated for D substitution at H sites shown in bold letters.

Additional References and Notes

37. W. Jones, J. Leigh, F. Mayer, C. Woese, R. Wolfe, *Methanococcus jannaschii* sp. nov., an extremely thermophilic methanogen from a submarine hydrothermal vent, *Arch. Microbiol.* **136**, 254–261 (1983).
38. W. E. Balch, G. Fox, L. Magrum, C. Woese, R. Wolfe, Methanogens: reevaluation of a unique biological group., *Microbiol. Rev.* **43**, 260 (1979).
39. L. C. Stewart *et al.*, *Methanocaldococcus bathoardescens* sp. nov., a hyperthermophilic methanogen isolated from a volcanically active deep-sea hydrothermal vent, *Int. J. Syst. Evol. Microbiol.* **in press** (2015), doi:10.1099/ijs.0.000097.
40. H. C. Ver Eecke, N. H. Akerman, J. A. Huber, D. A. Butterfield, J. F. Holden, Growth kinetics and energetics of a deep-sea hyperthermophilic methanogen under varying environmental conditions, *Environ. Microbiol. Reports* **5**, 665–671 (2013).
41. M. Alei *et al.*, Determination of deuterated methanes for use as atmospheric tracers, *Atmos. Environ.* **21**, 909–915 (1987).
42. S. Ono, B. Wing, D. Rumble, J. Farquhar, High precision analysis of all four stable isotopes of sulfur (^{32}S, ^{33}S, ^{34}S and ^{36}S) at nanomole levels using a laser fluorination isotope-ratio-monitoring gas chromatography mass spectrometry, *Chem. Geol.* **225**, 30–39 (2006).
43. G. Hut, *Consultants' group meeting on stable isotope reference samples for geochemical and hydrological investigations* (International Atomic Energy Agency, Vienna, Austria, 1987).
44. M. A. Webb, T. F. Miller, Position-specific and clumped stable isotope studies: Comparison of the Urey and path-integral approaches for carbon dioxide, nitrous oxide, methane, and propane, *J. Phys. Chem. A* **118**, 467–474 (2014).
45. X. Cao, Y. Liu, Theoretical estimation of the equilibrium distribution of clumped isotopes in nature, *Geochim. Cosmochim. Acta* **77**, 292–303 (2012).
46. Q. Ma, S. Wu, Y. Tang, Formation and abundance of doubly-substituted methane isotopologues ($^{13}CH_3D$) in natural gas systems, *Geochim. Cosmochim. Acta* **72**, 5446–5456 (2008).
47. R. K. Thauer, Biochemistry of methanogenesis: a tribute to Marjory Stephenson: 1998 Marjory Stephenson Prize Lecture, *Microbiology* **144**, 2377–2406 (1998).
48. J. M. Hayes, Fractionation of carbon and hydrogen isotopes in biosynthetic processes, *Rev. Mineral. Geochem.* **43**, 225–277 (2001).
49. J. D. Hermes, S. W. Morrical, M. H. O'Leary, W. Cleland, Variation of transition-state structure as a function of the nucleotide in reactions catalyzed by dehydrogenases. 2. Formate dehydrogenase, *Biochemistry* **23**, 5479–5488 (1984).
50. D. Roston, A. Kohen, Elusive transition state of alcohol dehydrogenase unveiled, *Proc. Natl. Acad. Sci. U. S. A.* **107**, 9572–9577 (2010).
51. M. Scharschmidt, M. A. Fisher, W. Cleland, Variation of transition-state structure as a function of the nucleotide in reactions catalyzed by dehydrogenases. 1. Liver alcohol dehydrogenase with benzyl alcohol and yeast aldehyde dehydrogenase with benzaldehyde, *Biochemistry* **23**, 5471–5478 (1984).
52. S. Scheller, M. Goenrich, R. K. Thauer, B. M. Jaun, Methyl-coenzyme M reductase from methanogenic archaea: Isotope effects on the formation and anaerobic oxidation of methane, *J. Am. Chem. Soc.* (2013).
53. E. Cerrai *et al.*, in *Chem. Eng. Progr. Symposium Ser.*, (Laboratori CISE, Milan, Italy, 1954).
54. J. Horita, Carbon isotope exchange in the system CO_2-CH_4 at elevated temperatures, *Geochim. Cosmochim. Acta* **65**, 1907–1919 (2001).
55. S. Ono, B. Wing, D. Johnston, J. Farquhar, D. Rumble, Mass-dependent fractionation of quadruple stable sulfur isotope system as a new tracer of sulfur biogeochemical cycles, *Geochim. Cosmochim. Acta* **70**, 2238–2252 (2006).
56. J. Rolston, J. Den Hartog, J. Butler, The deuterium isotope separation factor between hydrogen and liquid water, *J. Phys. Chem.* **80**, 1064–1067 (1976).
57. H. Suess, Das Gleichgewicht H_2 + HDO = HD + H_2O und die weiteren Austauschgleichgewichte im System H_2, D_2 und H_2O, *Zeitschrift Naturforschung Teil A* **4**, 328 (1949).
58. J. Horita, Stable isotope thermometry: There is more to it than temperature, *Geochem. J.* **39**, 481–496 (2005).
59. J. Tekippe *et al.*, Rumen fermentation and production effects of *Origanum vulgare* L. leaves in lactating dairy cows, *J. Dairy Sci.* **94**, 5065–5079 (2011).
60. G. J. Bowen, J. R. Ehleringer, L. A. Chesson, E. Stange, T. E. Cerling, Stable isotope ratios of tap water in the contiguous United States, *Water Resour. Res.* **43** (2007).
61. M. Riedel, T. Collett, M. Malone, the Expedition 311 Scientists, in *Proceedings of the Integrated Ocean Drilling Program*, (2006), vol. 311.
62. A. D. Laderman, M. Brody, E. Pendleton, The ecology of Atlantic white cedar wetlands: a community profile, (1989).
63. B. P. Scandella, C. Varadharajan, H. F. Hemond, C. Ruppel, R. Juanes, A conduit dilation model of methane venting from lake sediments, *Geophys. Res. Lett.* **38** (2011).
64. C. Varadharajan, R. Hermosillo, H. F. Hemond, A low-cost automated trap to measure bubbling gas fluxes, *Limnol. Oceanogr. Methods* **8**, 363–375 (2010).
65. M. Crespo-Medina *et al.*, Environmental controls on microbial communities in continental serpentinite fluids, *Front. Microbiol.* **5**, 604 (2014).
66. B. Sherwood Lollar *et al.*, Hydrogeologic controls on episodic H_2 release from Precambrian fractured rocks—Energy for deep subsurface life on Earth and Mars, *Astrobiology* **7**, 971–986 (2007).
67. B. Sherwood *et al.*, Methane occurrences in the Canadian Shield, *Chem. Geol.* **71**, 223–236 (1988).

68. B. M. Didyk, B. R. Simoneit, Hydrothermal oil of Guaymas Basin and implications for petroleum formation mechanisms, *Nature* **342**, 65–69 (1989).
69. B. R. Simoneit, Hydrothermal petroleum: genesis, migration, and deposition in Guaymas Basin, Gulf of California, *Can. J. Earth Sci.* **22**, 1919–1929 (1985).
70. B. R. Simoneit, P. F. Lonsdale, Hydrothermal petroleum in mineralized mounds at the seabed of Guaymas Basin, *Nature* **295**, 198–202 (1982).
71. J. S. Seewald, K. W. Doherty, T. R. Hammar, S. P. Liberatore, A new gas-tight isobaric sampler for hydrothermal fluids, *Deep Sea Res. Pt. I* **49**, 189–196 (2002).
72. W. Shanks, J. Böhlke, R. Seal, in S. E. Humphris, R. A. Zierenberg, L. S. Mullineaux, R. E. Thomson, Eds. (Wiley Online Library, 1995), pp. 194–221.
73. B. B. Bernard, J. M. Brooks, W. M. Sackett, Light hydrocarbons in recent Texas continental shelf and slope sediments, *J. Geophys. Res. Oceans* **83**, 4053–4061 (1978).
74. B. B. Bernard, J. M. Brooks, W. M. Sackett, Natural gas seepage in the Gulf of Mexico, *Earth Planet. Sci. Lett.* **31**, 48–54 (1976).
75. J. Bigeleisen, M. G. Mayer, Calculation of equilibrium constants for isotopic exchange reactions, *J. Chem. Phys.* **15**, 261 (1947).
76. M. J. Frisch *et al.*, Gaussian 03, Revision D.01 (Gaussian Inc., Wallingford, Connecticut, 2004).
77. J. Horita, D. J. Wesolowski, Liquid-vapor fractionation of oxygen and hydrogen isotopes of water from the freezing to the critical temperature, *Geochim. Cosmochim. Acta* **58**, 3425–3437 (1994).
78. R. D. Bardo, M. Wolfsberg, A theoretical calculation of the equilibrium constant for the isotopic exchange reaction between water and hydrogen deuteride, *J. Phys. Chem.* **80**, 1068–1071 (1976).
79. B. Brunner, S. M. Bernasconi, A revised isotope fractionation model for dissimilatory sulfate reduction in sulfate reducing bacteria, *Geochim. Cosmochim. Acta* **69**, 4759–4771 (2005).
80. J. Farquhar, D. T. Johnston, B. A. Wing, Implications of conservation of mass effects on mass-dependent isotope fractionations: influence of network structure on sulfur isotope phase space of dissimilatory sulfate reduction, *Geochim. Cosmochim. Acta* **71**, 5862–5875 (2007).
81. P. H. Janssen, Influence of hydrogen on rumen methane formation and fermentation balances through microbial growth kinetics and fermentation thermodynamics, *Anim. Feed Sci. Tech.* **160**, 1–22 (2010).
82. I. Friedman, K. Hardcastle, Deuterium in interstitial water from deep-sea cores, *J. Geophys. Res. Oceans* **93**, 8249–8263 (1988).
83. M. Riedel, T. Collett, M. Malone, the Expedition 311 Scientists, *Proceedings of the Integrated Ocean Drilling Program* E. 311 Scientists, Ed. (2006).
84. Y.-S. Lin *et al.*, Towards constraining H_2 concentration in subseafloor sediment: A proposal for combined analysis by two distinct approaches, *Geochim. Cosmochim. Acta* **77**, 186–201 (2012).
85. E. L. Rowan *et al.*, Geochemical and isotopic evolution of water produced from Middle Devonian Marcellus Shale gas wells, Appalachian Basin, Pennsylvania, *Am. Assoc. Pet. Geol. Bull.* (2014).
86. N. R. Warner *et al.*, Geochemical evidence for possible natural migration of Marcellus Formation brine to shallow aquifers in Pennsylvania, *Proc. Natl Acad. Sci. U. S. A.* **109**, 11961–11966 (2012).
87. H. C. Urey, The thermodynamic properties of isotopic substances, *J. Chem. Soc.* **Apr**, 562–581 (1947).